IEEE Access
Multidisciplinary | Rapid Review | Open Access Journal

IEEE VEHICULAR TECHNOLOGY SOCIETY SECTION

Received December 30, 2021, accepted February 24, 2022, date of publication March 8, 2022, date of current version March 15, 2022.

Digital Object Identifier 10.1109/ACCESS.2022.3157285

Doppler Spectrum Measurement Platform for Narrowband V2V Channels

CARLOS A. GÓMEZ-VEGA[1], (Graduate Student Member, IEEE), JORGE CARDENAS[2], (Student Member, IEEE), JUAN C. ORNELAS-LIZCANO[2], CARLOS A. GUTIÉRREZ[2], (Senior Member, IEEE), MARCO CARDENAS-JUAREZ[2], (Senior Member, IEEE), JOSÉ M. LUNA-RIVERA[2], AND RUTH M. AGUILAR-PONCE[2], (Member, IEEE)

[1]Department of Engineering and CNIT, University of Ferrara, 44122 Ferrara, Italy
[2]Faculty of Science, Universidad Autónoma de San Luis Potosí, San Luis Potosí 78295, Mexico

Corresponding author: Carlos A. Gutiérrez (cagutierrez@ieee.org)

This work was supported in part by the Universidad Autónoma de San Luis Potosí under Grant C20-FAI-10-24.24.

ABSTRACT This paper describes the implementation of a Doppler spectrum measurement platform for narrowband frequency-dispersive vehicle-to-vehicle (V2V) channels. The platform is based on a continuous-wave (CW) channel sounding approach widely used for path-loss and large-scale fading measurements, but whose effectiveness to measure the Doppler spectrum of V2V channels is not equally known. This channel sounding method is implemented using general-purpose hardware in a configuration that is easy to replicate and that enables a partial characterization of frequency-dispersive V2V channels at a fraction of the cost of a dedicated channel sounder. The platform was assessed in a series of field experiments that collected empirical data of the instantaneous Doppler spectrum, the mean Doppler shift, the Doppler spread, the path-loss profile, and the large-scale fading distribution of V2V channels under realistic driving conditions. These experiments were conducted in a highway scenario near San Luis Potosí, México, at two different carrier frequencies, one at 760 MHz and the other at 2,500 MHz. The transmitting and receiving vehicles were moving in the same direction at varying speeds, ranging from 20 to 130 km/h and dictated by the unpredictable traffic conditions. The obtained results demonstrate that the presented measurement platform enables the spectral characterization of narrowband V2V channels and the identification of their Doppler signatures in relevant road-safety scenarios, such as those involving overtaking maneuvers and rapid vehicles approaching the transmitter and receiver in the opposite direction.

INDEX TERMS Doppler shift, Doppler spectrum, fading channels, radio-frequency propagation, vehicular communications.

I. INTRODUCTION

Vehicular communication systems are an emerging technology aimed at applications related to road safety, traffic management, and on-board infotainment services [1]–[8]. Early efforts to equip vehicles with communication capabilities focused on the development of dedicated short-range communication (DSRC) technologies. In the U.S. and Europe, the DSRC technology is based on the specifications of the IEEE 802.11 Standard [9]. These specifications encompass the protocols for wireless access in vehicular environments [3], [4], including vehicle-to-vehicle (V2V) and vehicle-to-infrastructure (V2I) communications in the 5.9 GHz band [9].

The associate editor coordinating the review of this manuscript and approving it for publication was Hassan Omar.

Japan has also contributed to the development of DSRC technology for vehicular communications [4]–[6]. In this country, local regulatory agencies issued specifications for vehicular networks in the 700 MHz band [10]. In recent years, the Third Generation Partnership Project (3GPP) defined specifications for vehicle-to-everything (V2X) communications based on the infrastructure of the long-term evolution (LTE) cellular network [11]–[13]. With the fast development of fifth-generation (5G) networks, the 3GPP updated those specifications and defined new use cases for V2X communications within the 5G ecosystem [14]. These cellular-based V2X communication protocols also adopt the 5.9 GHz band for direct V2V communications [7], [13], [14].

Regardless of the particular frequency bands and communication protocols, the design of vehicular communication

systems faces several technical challenges related to the transmission of information through the rapidly-changing and highly-dispersive vehicular channel [15], [16]. The vehicles' mobility, paired with the short-range communication links, produces rapid variations of the channel's response that compromise the system performance [17]–[23]. Moreover, depending on the propagation conditions, the transmitted signal can arrive at the receiver through multiple interactions with interfering objects in the environment, resulting in worse-than-Rayleigh fading [24]–[26]. Hence, a thorough understanding and a correct characterization of the vehicular channel are crucial for the efficient design of V2X communication systems.

Theoretical V2V channel models have been developed to characterize wireless propagation in vehicular environments [27]–[31]. Typically, these models are derived by making certain assumptions on the mobility conditions and propagation environments. For instance, V2V channel models have been often developed assuming uniform motion, i.e., vehicles moving with constant speed over linear trajectories [25], [32]. Since this assumption is not always valid in practice, recent research efforts are aiming at the formulation of V2V channel models with non-uniform motion, i.e., assuming acceleration components and non-linear trajectories [33]–[35]. Regarding the propagation environment, some assumptions are made on the distributions of interfering objects for particular scenarios [36]. Conventional approaches consider isotropic or non-isotropic distributions of interfering objects around the vehicles [21]. For more realistic scenarios, ray-tracing models provide accurate representations of the propagation environments by considering the exact positions and electromagnetic properties of the interfering objects [37].

Besides the theoretical characterization of V2X channels, empirical data are also needed to gain insights into the behavior of realistic channels [16], [38]–[41]. Empirical data are obtained following a specific channel sounding principle, e.g., continuous-wave (CW), direct pulse, or correlation-based [42], [43]. The selection of the sounding principle depends on the channel characteristics that need to be analyzed. For example, the frequency-dispersive characteristics of time-varying V2V channels require a sounding approach aimed at capturing traces of the channel's Doppler spectrum. In turn, a sounding method with a focus on the channel's power delay profile (PDP) is required for the analysis of the time-dispersive characteristics of frequency-selective V2V channels [44]. Most high-performance channel sounding platforms employ specialized equipment to sample the Doppler spectrum and/or the PDP with a high resolution (e.g., see [45]–[48]). While desirable, such platforms are rare assets, as their high cost and specific purpose make their purchase the least priority to most universities and research centers. This limitation creates a need for innovative solutions to construct V2V channel sounding platforms with more accessible general-purpose equipment.

In response to this need, this paper describes the implementation of a Doppler spectrum measurement platform for frequency-dispersive V2V channels. The platform is based on a narrowband channel sounding principle that employs an analog radio-frequency (RF) signal generator to transmit a CW probe signal and a spectrum analyzer (SA) to measure the channel's Doppler spectrum for a given carrier frequency. This measurement setup has been widely used for path-loss and large-scale fading measurements, e.g., see [49]. However, the effectiveness of such a setup to measure the Doppler spectrum of V2V channels is not equally known. The resulting measurement platform is easy to replicate since it comprises general-purpose hardware commonly available in universities and research centers. It is, therefore, adequate not only for research but also for educational purposes, e.g., to illustrate the Doppler effect in mobile radio communications to undergraduate and graduate students.

This paper is the culmination of our previous work presented in [50]. The scope and contributions of [50] are extended here as follows:

- We provide a detailed discussion of the theoretical foundations of our implementation. This discussion is intended to help the reader to understand how our implementation works, and to identify its capabilities and limitations. We bring attention to a practical issue that affects the computation of the Doppler spectrum and that passed unnoticed in [50]: the presence of artifacts due to cross-terms in the measured channel's spectrogram. Moreover, we discuss the configuration of the hardware parameters that set the tradeoff between acquisition time and Doppler frequency resolution.
- We present a methodology to pre-process the measured spectrograms and circumvent the limitations of generic RF hardware. In particular, we address: (i) the frequency drifts in the transmitted signal caused by the operation of the signal generator; and (ii) the artifacts caused by cross-terms in the measured spectrograms.
- Finally, to demonstrate the capabilities of our measurement platform, we present the results of a measurement campaign at 760 MHz and 2,500 MHz in a highway scenario near San Luis Potosí, México. The experiments were conducted on a highway since this is a diverse and challenging environment where the effects of high mobility and the unpredictable dynamics of vehicular traffic can be observed clearly. We analyze the empirical Doppler signatures of the V2V channel in relevant road-safety scenarios, namely those involving overtaking maneuvers and rapid vehicles approaching the transmitter and receiver in the opposite direction. In addition, we characterize the distributions of the instantaneous mean Doppler shift and Doppler spread, the path-loss profile, and the large-scale fading distribution. While our platform does not measure the time-dispersive characteristics of wideband V2V channels, the obtained results demonstrate that it successfully captures the Doppler profile of frequency-dispersive V2V channels in realistic driving conditions.

The remainder of the paper is organized as follows. Section II provides a review of related work. The theoretical background and the details of our implementation are discussed in Sections III and IV, respectively. Section V addresses the hardware configuration and describes the highway scenario in which we tested the platform. Section VI presents our Doppler spectrum measurement results. Section VII addresses the computation of the path-loss profile and large-scale fading distribution from the measured Doppler spectra. Finally, Section VIII summarizes our conclusion.

II. MOTIVATION AND RELATED WORK

Substantial research efforts have focused on measuring the V2V channel at 5.9 GHz. Most approaches to measuring V2V channels seek high time resolution due to the rapid fluctuations of the V2V channel [45]–[47]. Measurements in [45], [46], [51], and [52] were performed using a multiple-input multiple-output (MIMO) channel sounder based on a switched-array principle. This architecture employs rubidium clocks for time reference synchronization to record accurate versions of the channel response with a digital signal processor as an interface. Measurements in [47] were conducted using a sounding platform that employs a software-defined radio to generate an unmodulated version of the IEEE 802.11p signal [53]. The transmission of this signal is repeated during the experiment and sampled by a data acquisition card with a high sample rate. Furthermore, measurements at 700 MHz have been conducted using a sounding platform based on a pulse-compression technique [54]. This platform employs a real-time SA to record the channel response. In particular, these implementations have been employed to effectively analyze channel characteristics in both time and frequency domains. Nevertheless, the experiments are not easy to reproduce due to the stringent hardware requirements of the channel sounding platforms.

Although the analysis of the channel's delay domain properties is important, a partial characterization of the V2V channel only in the Doppler frequency domain is also relevant. Measurements in [55] and [56], follow a CW sounding principle using a vector spectrum analyzer to record the channel's Doppler spectrum. In this platform, the time information obtained by Global Positioning System (GPS) receivers is employed for data synchronization. In particular, CW sounding principles have been mainly employed for the characterization of attenuation effects through zero-span measurements. However, the accuracy of these measurements is compromised when the signal generator is subject to frequency drifts due to temperature effects. This practical issue can be solved by increasing the frequency span to a few Hertz and correcting the observed drifts. Furthermore, such a solution can also be harnessed to measure the channel's Doppler spectrum by further increasing the frequency span. The CW sounding principle has two main advantages: (i) CW channel sounders might have simple architectures; and (ii) CW sounding platforms have sampling rates that enable continuous data acquisition over long trajectories.

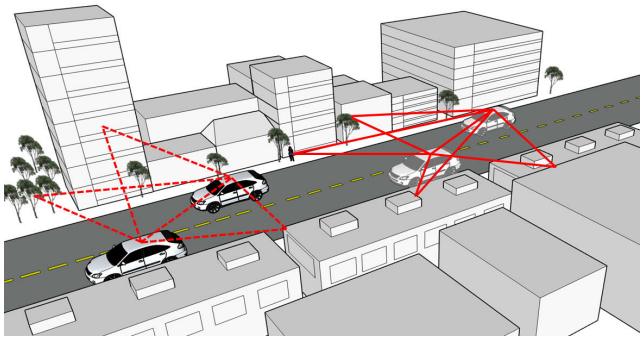

FIGURE 1. Time-varying multipath propagation in vehicular environments (red-solid lines: propagation paths at time instant $t = t_1$, red-dashed lines: propagation paths at time instant $t = t_2$).

While most channel sounders for V2V channels have stringent hardware requirements [45]–[47], [55], [56], general-purpose devices can be used to implement simpler architectures. In contrast to dedicated channel sounding platforms, the reconfiguration of general-purpose devices is straightforward and enables users to perform tests at different frequencies. The characterization of V2V channels at different frequencies is particularly relevant since the defined carriers might differ for different communication protocols (e.g., see [10], [13], [14], [53]).

III. PRELIMINARIES

In this section, we describe the theoretical foundations of our measurement platform. We discuss the main concepts of the V2V channel response and present the CW sounding principle harnessed in our implementation.

A. THEORETICAL BACKGROUND

In a vehicular radio communication system, the received signal is the superposition of multiple replicas of the transmitted signal that arrive at the receiver over different propagation paths, one of which can be a line-of-sight (LOS) path, as illustrated in Fig. 1. Hence, by neglecting the effects of additive noise, the received multipath signal can be modeled in the complex base-band equivalent by

$$y(t) = \sum_{n=1}^{N(t)} g_n(t) e^{-j[2\pi f_c \tau_n(t) + \theta_n(t)]} x(t - \tau_n(t)). \tag{1}$$

In this equation, $x(t)$ stands for the transmitted signal, f_c is the carrier signal frequency, $N(t)$ denotes the number of replicas of $x(t)$ that arrive at the receiver at the time instant t, whereas $g_n(t)$, $\theta_n(t)$, and $\tau_n(t)$ are the instantaneous attenuation factor, phase shift, and propagation delay of the nth received replica. The latter four parameters are characterized by time-dependent variables since the propagation conditions in vehicular environments may change at any moment due to the vehicles' high mobility and the short-range communication link (see Fig. 1).

In turn, the V2V channel can be modeled by a linear time-varying (LTV) system. An LTV system is uniquely characterized by its impulse response, $h(t;\tau)$, or equivalently, by its frequency response, $H(t;f) = \int_{-\infty}^{\infty} h(t;\tau)e^{-j2\pi f\tau}\,\mathrm{d}\tau$ [57]–[59]. Since (1) is the output of an LTV system to an input $x(t)$, i.e., $y(t) = h(t;\tau) * x(t)$ with $*$ denoting the convolution operation, we can characterize the V2V channel by

$$h(t;\tau) = \sum_{n=1}^{N(t)} g_n(t)e^{-j[2\pi f_c\tau_n(t)+\theta_n(t)]}\delta(\tau-\tau_n(t)) \quad (2)$$

$$H(t;f) = \sum_{n=1}^{N(t)} g_n(t)e^{-j[2\pi (f_c+f)\tau_n(t)+\theta_n(t)]} \quad (3)$$

where $\delta(t)$ denotes the Dirac delta function. Equation (3) shows that the V2V channel is a linear system whose response varies not only in the time domain, but also in the frequency domain. The channel's time and frequency variations cause a spectral dispersion of the transmitted signal. In particular, the channel's variation in time causes dispersion in the frequency domain, whereas its frequency variations cause dispersion in the time domain [44]. These effects can be analyzed in the joint domain of the Doppler frequency variable, ν, and the delay variable, τ, by the Doppler-delay spreading function $s(\nu;\tau) = \int_{-\infty}^{\infty}\int_{-\infty}^{\infty} H(t;f)e^{-j2(\nu t-f\tau)}\,\mathrm{d}t\,\mathrm{d}f$. Alternatively, the channel dispersion can be analyzed in the Doppler domain on the grounds of the frequency-dependent Doppler-spread function

$$D(\nu;f) = \int_{-\infty}^{\infty} H(t;f)e^{-j2\pi\nu t}\,\mathrm{d}t \quad (4)$$

or in the delay domain, with respect to $h(t;\tau)$, which is a time-dependent delay-spread function dual to $D(\nu;f)$. We refer the reader to [58]–[61] for a detailed discussion on the system functions of mobile radio channels.

From the definition of $h(t;\tau)$, it follows that the response of the V2V channel can be measured in practice by transmitting a signal of a very short duration, e.g., those designed for spread spectrum and ultra-wideband communications [62]–[65]. Also, from the definition of $H(t;f)$, the channel response can be measured by transmitting multiple unmodulated complex sinusoids of different frequency, either sequentially (as in frequency-hopping communication systems [66], [67]) or simultaneously (as in orthogonal frequency division multiplexing systems [47], [48], [68], [69]). However, the transmission of these signals relies on costly equipment, such as vector waveform/function generators, and their detection requires the implementation of sophisticated receivers that rely on accurate synchronization with the transmitter.

B. NARROWBAND CHANNEL SOUNDING PRINCIPLE

The complexity and high cost of implementing a V2V channel sounder are further exacerbated by the difficulty in measuring the channel response with a high resolution in time and frequency. An alternative to simplify the channel sounder architecture is to measure the channel response only in one dimension. For mobile communications in rapidly time-varying channels, the time-domain response is critical to assess the impact of signal dispersion in the Doppler frequency domain [70]–[73]. To measure the response of the V2V channel only in the time domain, it suffices to transmit a CW probe waveform, $x(t) = 1$, i.e., an unmodulated carrier signal. Thereby, the received signal is given by

$$c(t) = \sum_{n=1}^{N(t)} g_n(t)e^{-j[2\pi f_c\tau_n(t)+\theta_n(t)]}. \quad (5)$$

where $c(t)$ can be identified as the channel complex envelope (CCE) since $c(t) = H(t;f)\big|_{f=0}$. The reception process can be simplified further if the channel's instantaneous power, $z(t) = |c(t)|^2$, is measured instead of the CCE. This narrowband channel sounder can be implemented with general-purpose hardware, such as an analog RF signal generator and an SA. Measurement platforms of this type are typically employed to gather empirical information about the fading statistics of narrowband channels. However, the same platform can be employed to characterize the channel dispersion in the Doppler frequency domain. To show this, we note that an spectrum analyzer (SA) produces traces of the received signal's spectrogram

$$S(\nu,t') = |Y(\nu,t')|^2 \quad (6)$$

where the variable t' denotes a particular observation time instant, and

$$Y(\nu,t') = \int_{-\infty}^{\infty} c(t)w(t-t')e^{-j2\pi\nu t}\,\mathrm{d}t \quad (7)$$

is the short-time Fourier transform (STFT) of $c(t)$, where $w(t)$ is a real-valued even function given such that $w(t) > 0$ for $|t| < T_0/2$, $w(t) = 0$ for $|t| > T_0/2$, $\int_{-\infty}^{\infty} w^2(t)dt = 1$, and $T_0 > 0$ [74]. In practice, the constant quantity T_0 can be associated to the sweep time of an SA. Assuming that the number of multipath components of the channel response remains constant within an observation interval of length T_0, we can write the STFT of the CCE for a given discrete time, $t'_k = kT_0$, for $k \in \mathbb{Z}$, as

$$Y(\nu,t'_k) = \sum_{n=1}^{N_k} g_{k,n}e^{-j\theta_{k,n}} \times \int_{-\infty}^{\infty} w(t-t'_k)e^{-j2\pi[\nu t+f_c\tau_{k,n}(t)]}\,\mathrm{d}t. \quad (8)$$

In this equation, N_k is the number of resolvable multipath components of $c(t)$ within the kth observation interval, $\left(k-\frac{1}{2}\right)T_0 < t' \leq \left(k+\frac{1}{2}\right)T_0$, whereas $g_{k,n}$, $\theta_{k,n}$, and $\tau_{k,n}(t)$ are the corresponding attenuation factor, phase shift, and time-varying propagation delay, respectively, of the nth received replica of $x(t)$ within the kth observation interval. Assuming also that the received signal is given by the

superposition of N_k electromagnetic plane waves, the time-varying propagation delays $\tau_{k,n}(t)$ are equal to

$$\tau_{k,n}(t) = \tau_{k,n}^{(0)} - t\frac{\nu_{k,n}}{f_c} \tag{9}$$

where $\tau_{k,n}^{(0)}$ and $\nu_{k,n}$ are the initial propagation delay and the Doppler shift, respectively, of the nth plane wave received within the kth observation interval [75]. In particular, the Doppler shift $\nu_{k,n}$ can be expressed as

$$\nu_{k,n} = f_{k,n}^{S} + \frac{\dot{f}_{k,n}^{A}(t)}{2} \tag{10}$$

where $f_{k,n}^{S}$ and $\dot{f}_{k,n}^{A}(t)$ are Doppler shifts caused by the vehicles' speed and acceleration for the nth plane wave received within the kth observation interval, respectively. The first component depends on the initial speeds of the vehicles, whereas the second term is a time-varying quantity that depends on the vehicles' acceleration profiles.

Thereby, we have

$$Y(\nu, t_k') = \sum_{n=1}^{N_k} g_{k,n} W(\nu - \nu_{k,n}) e^{j\left[2\pi\left(\nu t_k' - f_c\tau_{k,n}^{(0)}\right) - \theta_{k,n}\right]} \tag{11}$$

where $W(\nu)$ is the Fourier transform of the windowing function $w(t)$. The STFT of the CCE provides a time-dependent description of the channel dispersion in the Doppler domain. The function $Y(\nu, t_k')$ is similar in that regard to the frequency-dependent Doppler-spread function defined in (4). In fact, if the number of multipath components is constant for all t, then, in the limit when $T_0 \to \infty$, one can verify that $Y(\nu, 0) = D(\nu, 0) = \sum_{n=1}^{N_0} g_n e^{j\left[2\pi f_c \tau_n^{(0)} - \theta_n\right]} \delta(\nu - \nu_n)$. From (6) and (11), it follows that the spectrogram of the CCE is equal to

$$S(\nu, t_k') = S_A(\nu, t_k') + S_C(\nu, t_k') \tag{12}$$

where the spectral function

$$S_A(\nu, t_k') = \sum_{n=1}^{N_k} g_{k,n}^2 W^2(\nu - \nu_{k,n}) \tag{13}$$

contains the auto-terms of the CCE. This function has a clear physical meaning as it can be interpreted as the channel's time-varying Doppler spectrum [74]. In turn, the function

$$S_C(\nu, t_k') = \sum_{n=1}^{N_k} \sum_{\substack{m=1 \\ m\neq n}}^{N_k} g_{k,m} g_{k,n} W(\nu - \nu_{k,m}) W(\nu - \nu_{k,n}) \times e^{j\left[2\pi f_c\left(\tau_{k,m}^{(0)} - \tau_{k,n}^{(0)}\right) + \left(\theta_{k,m} - \theta_{k,n}\right)\right]} \tag{14}$$

contains the cross-terms of $S(\nu, t_k')$. In contrast to $S_A(\nu, t_k')$, $S_C(\nu, t_k')$ does not have a physical meaning since the cross-terms are artifacts caused by the windowing function $w(t)$. In the case of a super-heterodyne SA, the cross-terms are also related to the dynamic range of the frequency mixers [76].

Equations (12)–(14) show that the Doppler spectrum of a V2V channel can be measured in practice by employing a narrowband channel sounder that follows the principle described in this section. One of the challenges of implementing such a platform is to find the value of the SA's sweep time that maximizes the contribution of the spectrogram's auto-terms and minimizes that of the cross-terms. It can be shown that the spectrogram's cross-terms vanish in the limit when $T_0 \to \infty$ [74]. However, this asymptotic scenario is of little relevance in practice since the sweep time of an SA cannot extend to infinity. Moreover, short sweep times are required to ensure that the time variations of $N(t)$, $g_n(t)$, and $\theta_n(t)$ are negligible within the observation window of length T_0. Nevertheless, the sweep time cannot be too short either since this will reduce the SA's capability to resolve the spectrogram's auto-terms that are in close proximity to each other. There is, therefore, a critical tradeoff in finding a proper value for the sweep time.

In practice, the sweep time is determined by the resolution bandwidth (RBW), video bandwidth (VBW), and frequency span [76]. In modern SAs, such parameters are coupled to avoid measurement errors. Therefore, setting a subset of parameters will update the others automatically. For example, the VBW is coupled linearly with the RBW. In the case of measuring CW probe signals, the RBW should be set to the smallest possible value [77]. Nevertheless, this configuration will affect the time resolution significantly since decreasing the RBW will increase the sweep time [76], [77]. Therefore, we need to find a compromise between a sufficiently small RBW (typically a few Hertz) and a suitable sweep time.

IV. THE MEASUREMENT PLATFORM

In this section, we present the implementation of our Doppler spectrum measurement platform for frequency-dispersive V2V channels. We describe the main components and considerations to assemble the transmitter and receiver stations according to the theoretical concepts revised in the previous section. The discussion is intended to guide the interested readers to replicate the platform with their own hardware.

A. IMPLEMENTATION

The particular devices in our implementation are the Keysight N9310A radio-frequency (RF) signal generator [78], and the Keysight Fieldfox N9913A in SA mode [79]. The N9310A RF signal generator enables the transmission of an RF wave in frequencies that range from 9 kHz to 3 GHz. The highest power level that this device provides is 20 dBm. Since this is an RF device built with non-ideal components, the probe signal may be subject to frequency drifts due to temperature effects. An approach to tackle this particular issue will be discussed in the next subsection.

The N9913A is a portable device that includes the SA mode. This device can measure signals with frequencies that range from 30 kHz to 4 GHz. The proper configuration of the SA is important for this specific application

TABLE 1. List of materials and hardware for the measurement platform.

Materials	Company	Model/Description
SA	Keysight	FieldFox N9913A
RF signal generator	Keysight	N9310A
GPS receivers	Digilent	PmodGPS
Antennas	Generic	Half wavelength dipoles at 760 MHz and 2,500 MHz
Cabling	Generic	RG-6 cables of different lengths
Adapters	Generic	N-type male to F-type female
Laptops	Generic	Control computers equipped with MATLAB© software
Ethernet cable	Generic	For communication between a control computer and the SA
Video cameras	Generic	For recording the changes of the propagation scenario

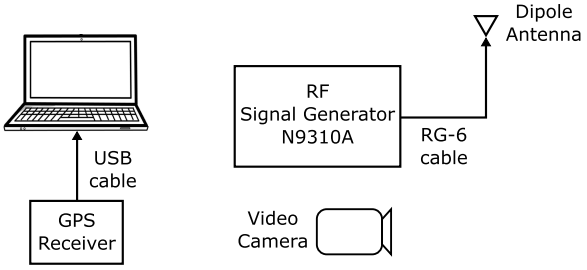

FIGURE 2. Block diagram of the transmitter station.

since it involves the tradeoff between time and frequency resolution. The flexibility of these two devices enables us to measure the Doppler spectra of V2V channels at different frequencies by reconfiguring some of the hardware parameters.

In addition to the described devices, the measurement platform requires pairs of antennas at specific frequencies, cabling, and adapters. Furthermore, other components are needed to gather complementary information to analyze the V2V channel characteristics effectively. In particular, GPS receivers are crucial to obtain time-stamped position information of the vehicles. This information is used to determine the instantaneous separation distances among vehicles, which are particularly important to describe the path-loss profile. Laptop computers are required to record the position information and control the measurement hardware. Video cameras are also useful in this context to record how the propagation scenario changes during the experiments, e.g., to establish the time intervals measured under LOS conditions. Table 1 summarizes the list of employed materials.

A block diagram of the transmitter station is illustrated in Fig. 2. The CW probe signal is produced by the N9310A RF signal generator and transmitted by a dipole antenna at 760 MHZ (or 2,500 MHz). In particular, we set the carrier frequency to 760 MHZ (or 2,500 MHz) and the RF output level to 20 dBm. Before performing any experiment, we power on, configure, and allow this device to warm up for half an hour. The warm up reduces the effects

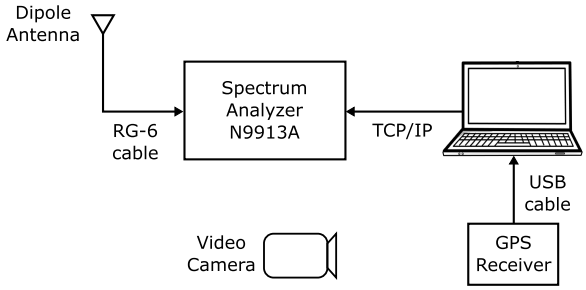

FIGURE 3. Block diagram of the receiver station.

of temperature on the frequency drift of the probe signal during the experiments. Once turned on, this device will continuously transmit the probe signal without requiring any control device. We equip this station with a GPS receiver and a laptop to record the position information. Moreover, we consider a video camera in this station to record the propagation scenario from the transmitter perspective.

A block diagram of the receiver station is illustrated in Fig. 3. The signal is received by a dipole antenna at 760 MHz (or 2,500 MHz) connected to the N9913A in SA mode. This station is also equipped with a GPS receiver, a laptop, and a video camera. The laptop in this station runs a MATLAB script to configure the SA's parameters automatically via the TCP/IP protocol. We use the same protocol to initiate and stop the data recording in the SA by sending control commands. In particular, the measured data was stored in the SA's internal memory since this required less time than recording directly in the computer by querying the spectrogram's data via the TCP/IP protocol. While the SA records the spectrogram's data, the laptop stores the time-stamped position information from the GPS receiver. The SA is configured according to the parameters shown in Table 2. The central frequency is set to the frequency of the probe signal (760 MHz or 2,500 MHz). We consider a frequency span of 1,500 Hz for the probe signal at 760 MHz, and of 2,000 Hz for the signal at 2,500 MHz. We also consider the maximum number of frequency span sample points (1001) supported by the SA to measure the Doppler spectrum of V2V channels with sufficient resolution. In low mobility conditions, the frequency span can be further reduced according to the considered speed range. As discussed in the previous section, the choice of the RBW compromises the sweep time. Since the measured spectrogram is stored in the SA's internal memory (or directly in the computer), the RBW should be set also taking into account the recording time. We set the RBW to 10 Hz since it enables suitable sweep times to perform the experiments without compromising the capability to resolve the spectral components. In this regard, the aim is to find a small value of the RBW that avoids the distortion of a pure tone measured in controlled conditions and does not yield a large sweep time. The average sweep time obtained in this setting was 0.27 s, but the total acquisition time including the latency due to data recording in the SA internal memory was about 0.40 s.

TABLE 2. List of parameters for the configuration of the SA.

Parameter	Value
Central frequency	760 MHz 2,500 MHz
Frequency span	1,500 Hz (@760 MHz) 2,000 Hz (@2,500 MHz)
Sample points	1001
RBW	10 Hz
Attenuation	0 dB
Pre-amp	On

B. PRACTICAL ASPECTS

In practice, the measured spectrograms are subject to several impairments caused by the non-ideal RF components of the hardware. We address here two practical aspects of our implementation: (i) the frequency drifts of the transmitted signal due to temperature effects on the RF signal generator; and (ii) the presence of artifacts caused by the cross-terms in the measured spectrograms.

To compensate for the practical issues of our platform, we conducted reference measurements in controlled laboratory conditions and in-field with static vehicles. The first control measurements were taken with the output of the RF signal generator connected directly to the input of the SA while setting the transmitting power to -40 dBm. We attenuated the transmitting power for such experiments to prevent an overload in the SA's input. Figure 4 shows a 500 Hz window of a spectrogram measured at 2,500 MHz over 210 s. This spectrogram illustrates the two practical issues mentioned above. The first effect is observed in the deviation of the received signal from the central frequency over time. The second effect is observed in the undesirable contributions above noise level that appear around the carrier frequency (yellow lines). Note that the probe signal is not a monochromatic signal, as it does not have a zero bandwidth. It occurs since, in practice, the signal spectrum is widened over a few Hertz due to filtering and time windowing stages. In the following, we discuss each issue separately and our approach to addressing them in the pre-processing stage.

The frequency drifts of the transmitted signal are caused by the continuous operation of the RF signal generator. The frequency drifts of the spectrogram with respect to the central frequency are shown in Fig. 5. This plot shows that the carrier frequency of the received signal shifts to negative frequencies in this particular experiment. The frequency drift appears to change linearly with small variations due to the uncertainty of the signal detection in the SA. This issue can be compensated in practice by taking control measurements during short intervals at the beginning and the end of each experiment run. The transmitter and receiver should remain completely stationary during such control intervals to avoid the probe signal's spectral dispersion caused by the combined effects of multipath and the Doppler effect. The spectrogram's snapshots recorded with the vehicles in static conditions

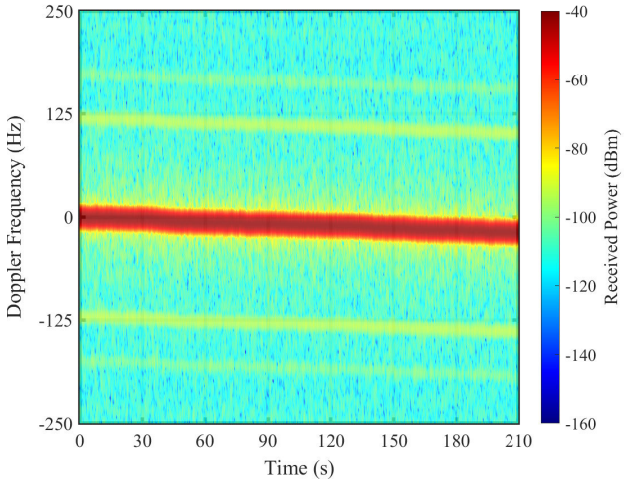

FIGURE 4. A measured spectrogram to illustrate the practical issues of our implementation. The carrier frequency of the probe signal is 2,500 MHz.

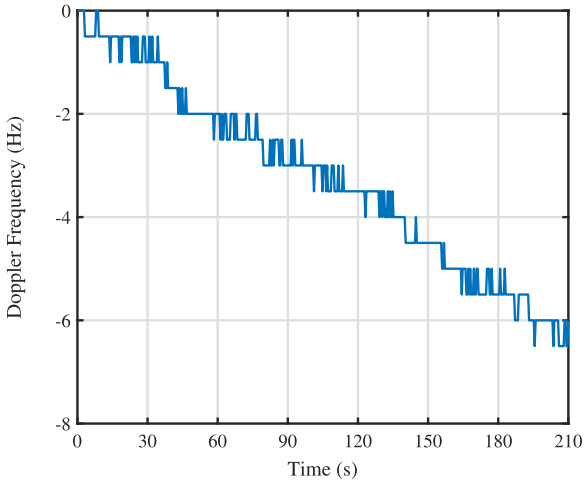

FIGURE 5. Frequency drift of a received signal over time.

allow to identify the initial and final trend of the frequency drift. The rest of the snapshots, obtained with the vehicles in motion, are realigned employing frequency drift estimates obtained from a piece-wise linear regression of the reference head and trail snapshots.

As discussed in the previous section, the cross-terms of the measured spectrogram are undesirable artifacts that corrupt the Doppler spectrum. The presence of such artifacts can be masked by the additive noise. The effects of the cross-terms are illustrated in Fig. 6, which shows a snapshot of the spectrogram presented in Fig. 4 with the frequency drift corrected. Figure 7 presents a time average of the spectrogram shown in Fig. 4 after the correction of the frequency drift. The average operation smooths the additive noise's variations around its average power and highlights the presence of artifacts around the carrier frequency. In practice, these artifacts can mask propagation effects that are important to the statistical analysis of the measured V2V channels. Our approach to address this issue consists of computing the correlation of

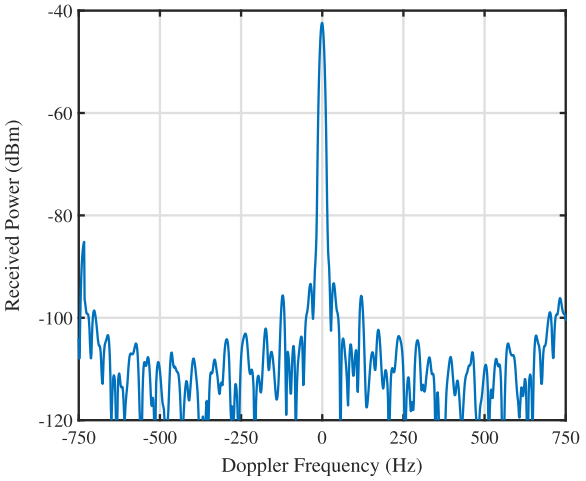

FIGURE 6. A snapshot of a measured spectrogram. The carrier frequency of the probe signal is 2,500 MHz.

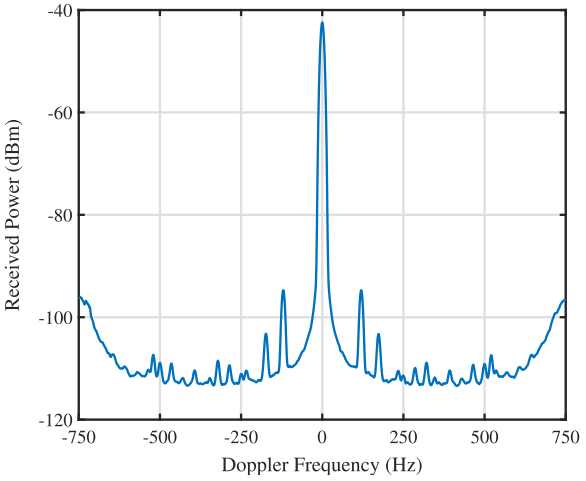

FIGURE 7. Averaged spectrogram mask computed by averaging over 180 snapshots. The contributions of the spectrogram's cross-terms appear as spikes above the noise level.

each snapshot in the measured spectrogram with a proper spectrogram mask. The spectrogram masks are obtained by averaging snapshots of spectrograms measured in laboratory conditions at the corresponding carrier frequencies, such as that shown in Fig. 7. To complete the pre-processing stage, we readjust the amplitudes and scale them to the original values in the measured spectrogram. Finally, we apply a threshold to clip the noise level. Such a threshold can be set equal to the average noise level or can be determined empirically by inspecting the results. After addressing the two practical aspects by pre-processing the raw data, we obtain the spectrogram $\tilde{S}(\nu, t'_k)$ that can be used to compute the channel's statistics.

V. THE MEASUREMENT CAMPAIGN

In this section, we discuss how to assemble the measurement platform on the test vehicles and how we perform a measurement campaign. Moreover, we discuss the particular scenario where we performed our experiments.

A. THE MEASUREMENT SETUP

First, the RF signal generator and the SA are installed on the vehicles' main storage compartments using base plates. Moreover, the antennas and GPS receivers are placed on the vehicles' roofs using permanent magnets. Then, we connect the antennas and GPS receivers to the corresponding devices. Finally, we configure the hardware according to the discussion in Section IV-A and allow it to warm up before performing any experiment. Each test vehicle is equipped with a portable power generator that supplies the devices.

To perform the experiments, a passenger in each vehicle is in charge of a laptop computer. The passenger in the receiver station controls the SA and coordinates the experiments. In the transmitter station, the passenger with the computer receives the instructions to initiate or stop the acquisition of the position information. We synchronize the position information offline using the time stamp of each sample. Besides, one passenger in each vehicle records the video of the propagation scenario. The role of these two passengers is to take notes and make voice comments on the propagation and traffic conditions that we observe during the experiments, e.g., the availability of LOS conditions, the speed of the corresponding vehicle, and what maneuvers are the drivers attempting. Such notes and comments were used for the synchronization between measurements and video recordings, e.g., the starting time of each experiment.

B. THE MEASUREMENT SCENARIO

The measurement campaign was performed on the Mexican Federal Highway 80D in a mountainous area on the outskirts of the city of San Luis Potosí, México. The route over this highway is shown in Fig. 8, where the labels *A* and *B* indicate the route's starting and ending points, respectively. This route spans 25 km and is completed in approximately 15 minutes, depending on traffic conditions. A total of sixteen circuits were completed for the measurements, eight with the probe signal centered at 760 MHz and eight more with the signal at 2,500 MHz. During the experiments, the test vehicles were moving in the same direction. The receiver was most of the time in front of the transmitter, and occasionally and momentarily, they changed position to perform overtaking maneuvers. Both vehicles seek to maintain a velocity between 80 and 120 km/hr and a separation distance between 100 and 250 m. However, they were subject to arbitrary velocity variations caused by the changing traffic conditions over the route. Also, the separation distance was increased to up to 500 m in some sections of the road to expand our assessment of path-loss and large-scale fading.

The relevant road sections can be described as follows:

- Scenario #1: Road sections that pass through mountain cutouts. In these sections, tall and long rock walls carved through the mountain are found on both sides of the road. Some of the walls are long enough to flank both vehicles at the same time, as illustrated in Fig. 9(a), whereas others are shorter and border only one vehicle

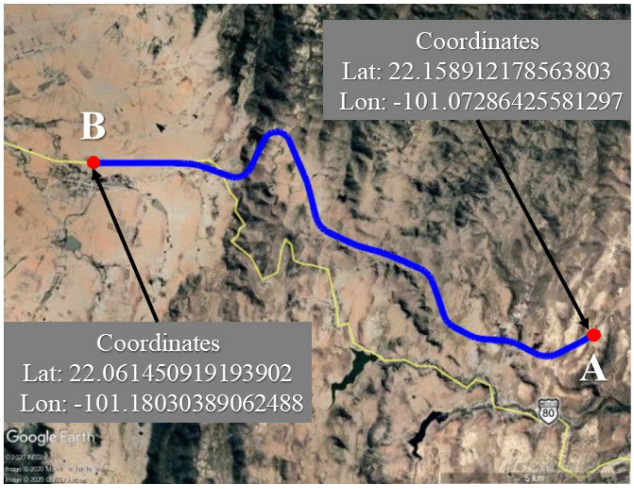

FIGURE 8. Map showing the route of the measurement campaign.

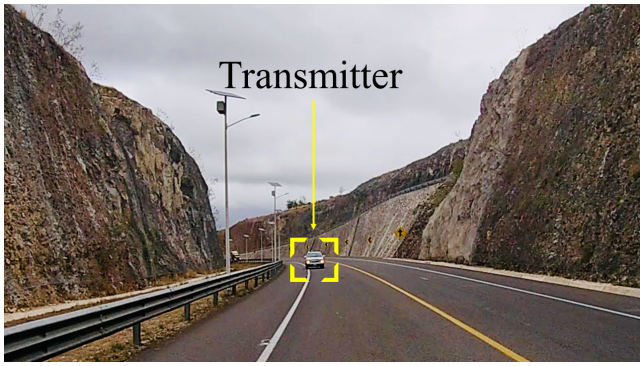

(a) Receiver camera

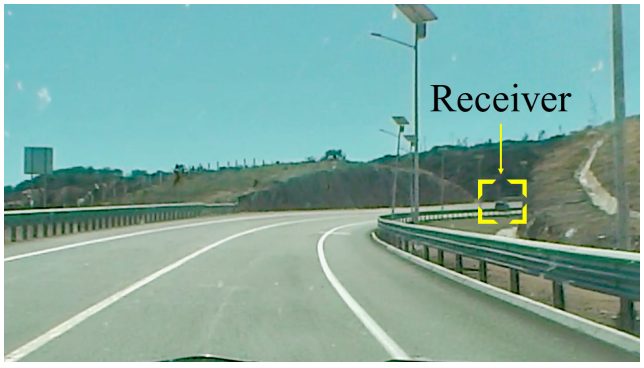

(b) Transmitter camera

FIGURE 9. Two sections of the road with steep rock walls on both sides.

at a time, as shown in Fig. 9(b). The rock walls have a slight inclination, and produce strong multipath around the transmitter and/or the receiver. Multipath stemming from double scattering or double reflections is possible in this scenario, as discussed in the following subsection. Some of these road sections also pass under bridges, e.g., see Fig. 10. These elevated structures produce strong reflections and a large Doppler shift, as the signals reflected off the bridge arrive from the front (or the back) of the receiving vehicle.

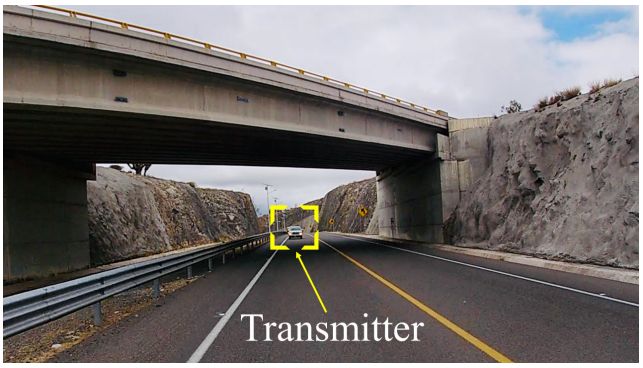

FIGURE 10. Section of the road with steep mountains on both sides and an under bridge pass (Receiver camera).

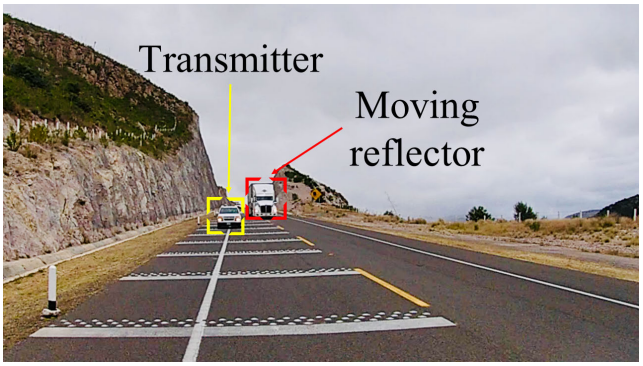

(a) Receiver camera

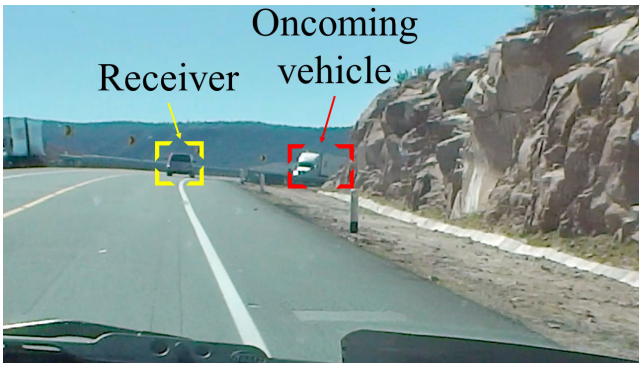

(b) Transmitter camera

FIGURE 11. Two sections of the road with a steep rock wall on one side.

- Scenario #2: Road sections that go around the mountains. In these sections, the vehicles are flanked by a rock wall only on one side, whereas the other side is clear and goes downwards following the mountain's slope, as shown in Fig. 11. Reflections off the rock wall produce strong multipath with a highly non-isotropic profile, implying that the mean Doppler shift of the channel will be different from zero.
- Scenario #3: Road sections in the open field. Reflectors and scattering clusters of large dimensions (such as rock walls or hillsides) are far off, as illustrated in Fig. 12. Weak multipath stemming from the irregular terrain prevails in these road sections. However, the multipath is

occasionally intensified by strong replicas of the probe signal reflected by man-made objects, such as road signs and metallic safety barriers.

The road also presents sections with sharp curves bordered by steep mountain walls. These curved sections are interesting since the walls can hinder a prompt visual detection of oncoming vehicles, as in the scenario shown in Fig. 11(b). Furthermore, such sharp curves can obstruct the LOS path between communicating vehicles. This latter situation is illustrated in Fig. 9(b), where the receiver is about to lose LOS contact with the transmitter as both vehicles take a long curve stretch that passes through a mountain cutout. During the experiments, we observed LOS blockages also in straight sections of the road. These blockages were caused by vehicles of large dimensions that found themselves momentarily placed between the transmitter and the receiver, as in the instance shown in Fig. 12(b),

The traffic dynamics of the Federal Highway 80D allowed us to record the probe signal's spectral dispersion during overtaking maneuvers. The test vehicles performed these maneuvers on each other in a controlled sequence that was coordinated using portable two-way radios. Figure 12(a) shows the transmitting vehicle performing an overtaking on the receiving vehicle. In addition to these coordinated maneuvers, spontaneous overtaking, involving a third party and one of the test vehicles, were prompted arbitrarily by the traffic conditions. One of such non-coordinated maneuvers is depicted in Fig. 11(a), where a truck is overtaking the transmitting vehicle.

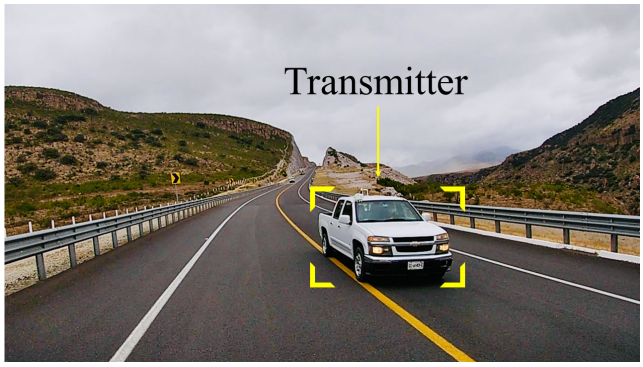

(a) Receiver camera

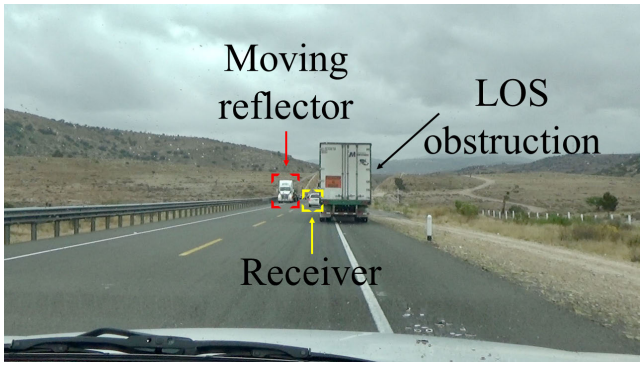

(b) Transmitter camera

FIGURE 12. Two sections of the road in open field with mountains in the distance.

VI. MEASUREMENT RESULTS OF THE DOPPLER SPECTRUM

This section presents the empirical Doppler spectrum recorded during our experiments. The discussion focuses on the relevant Doppler statistics of time-varying V2V channels. We describe the processing methods used to compute the Doppler spectrograms and the corresponding moments from the empirical data.

A. PRE-PROCESSING

Before computing the channel's statistics from the measured data, a data pre-processing stage is necessary to address the practical issues of our channel sounding platform that are discussed in Section IV-B. The pre-processing stage consists of the following actions:

1) Center the snapshots of the measured spectrogram, i.e., correct the frequency drifts due to temperature effects.
2) Compute correlation with a proper mask to mitigate the effects of cross-terms in the measured spectrogram.
3) Scale the processed spectrogram's values back to the original power levels.
4) Apply a noise floor threshold to set all values below this threshold to the same level.

Figures 13 and 14 show the raw spectrograms of two measurement runs, one at 760 MHz and the other at 2,500 MHz, respectively. In Fig. 13, the measurement route went from point A to point B (cf. Fig. 8), whereas in Fig. 14, it went from B to A. Both figures show the header and tail control snapshots that we used as a reference to correct the frequency drift due to temperature effects. This impairment, observed in both figures, does not change significantly over time. However, the received signal's frequency is deviated from the central frequency due to drifts in past observations.

The pre-processed version of the raw spectrograms in Figs. 13 and 14 are presented in Figs. 15 and 16, respectively. These sanitized spectrograms were obtained following the procedures described in Section IV-B for frequency drift correction and noise clipping. The frequency dispersion of the probe signal, which is caused by multipath propagation and the Doppler effect, can be observed clearly in Figs. 15 and 16. As soon as the vehicles start to move, part of the probe signal's power is spread out, forming a contour bounded by the instantaneous maximum Doppler shift, $\nu_{\max}^{sta}(t)$, due to static reflectors. This frequency shift is given by

$$\nu_{\max}^{sta}(t) = \frac{v_T(t) + v_R(t)}{\lambda} \tag{15}$$

where $v_T(t)$ and $v_R(t)$ denote the instantaneous speed of the transmitter and receiver, respectively [32]. The maximum Doppler shift is observed when the probe signal is reflected by an object located either in front (or nearly in front) of the receiver, or behind the transmitter. These propagation conditions are recurring in the route of our experiments due to the presence of traffic signs, rocky hillsides, or bridges. For

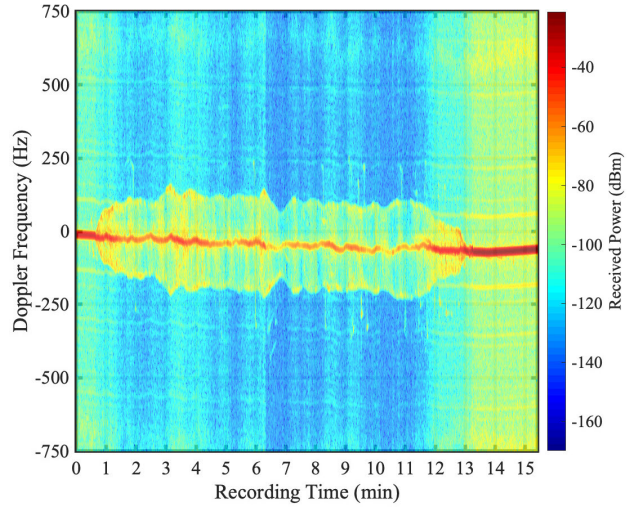

FIGURE 13. A raw spectrogram recorded at 760 MHz.

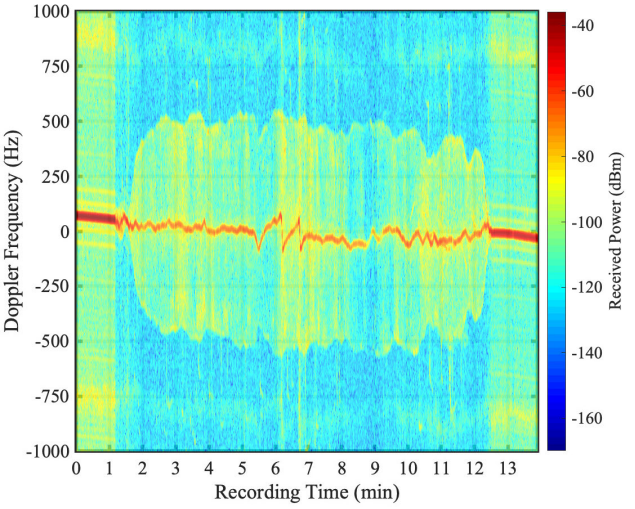

FIGURE 14. A raw spectrogram recorded at 2,500 MHz.

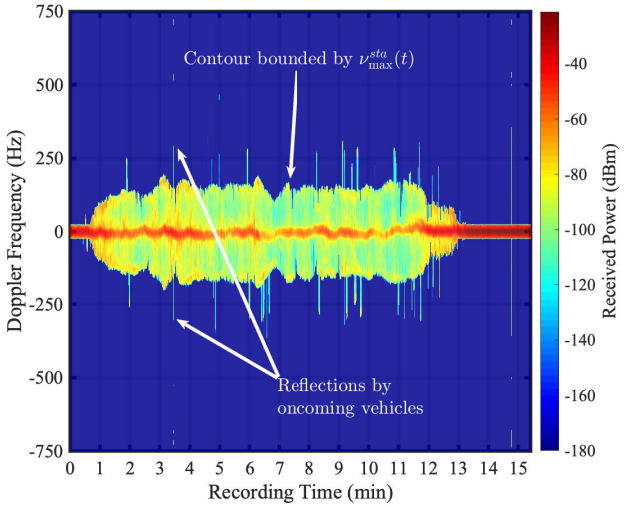

FIGURE 15. A pre-processed spectrogram recorded at 760 MHz.

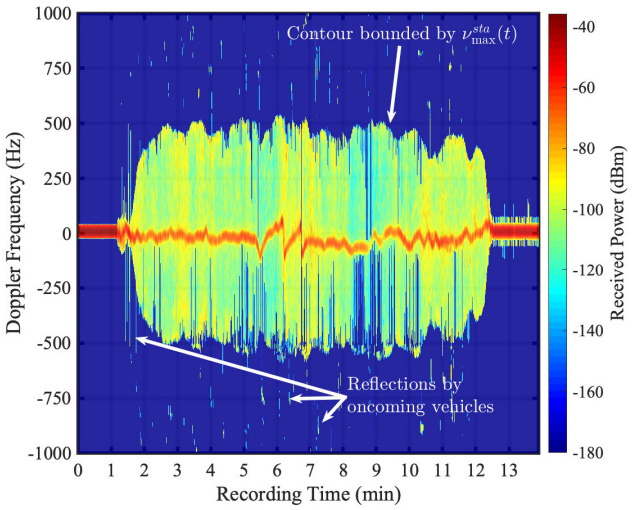

FIGURE 16. A pre-processed spectrogram recorded at 2,500 MHz.

the measurements at 760 MHz, the largest maximum Doppler shift was produced when the transmitting and receiving vehicles were moving at a speed of about 110 km/h, causing a peak value of $\nu_{\max}^{sta}(t)$ of around 169 Hz. Likewise, for the measurements at 2,500 MHz, the maximum Doppler shift was produced for $v_T(t) \approx v_R(t) \approx 120$ km/h, corresponding to $\nu_{\max}^{sta}(t) \approx 555$ Hz. The frequency dispersion of the probe signal changed frequently throughout the measurement route due to the traffic dynamics. Indeed, Figs. 15 and 16 show the spreading (and despreading) effects of the vehicles' acceleration (and deceleration) on the signal frequency dispersion. Such effects are more evident when the vehicles begin and conclude their transit, but can also be identified along the route by the unceasing widening and narrowing of the recorded spectrogram.

B. DOPPLER SIGNATURES OF RELEVANT ROAD SAFETY EVENTS

The spectrograms presented in Figs. 13–16 show that the measurement platform described in Section IV is capable of recording the frequency dispersion caused by multipath propagation and the Doppler effect. A close inspection of the measured spectrograms suggests that the platform allows recording the Doppler signatures of relevant events to road safety, as those produced by rapidly oncoming vehicles and overtaking maneuvers. Figure 17 exemplifies a common road event by extracting a segment of eleven seconds of the spectrogram in Fig. 15. This segment was recorded on an open-field road section when a large truck was approaching, passing by, and driving away. During this event, the transmitter and receiver vehicles always maintained a LOS path with the truck. Figure 18 presents three pictures of this event captured by the transmitter's video camera at the time instants at which: the reflection from the oncoming truck was detected (Fig. 18(a)), the truck and the receiver were side by side (Fig. 18(b)), and the truck was driving away and the reflected signal was about to disappear (Fig. 18(c)). Figure 19 shows the corresponding Doppler spectra of these three time

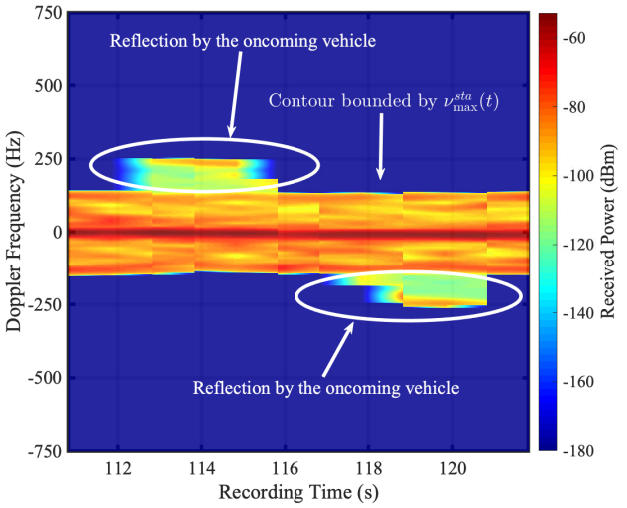

FIGURE 17. An interval of a pre-processed spectrogram recorded at 760 MHz during an event involving a rapidly oncoming vehicle in an open-field road segment.

instants. We can observe from Figs. 17 and 19 that the reflection of the oncoming truck produces a tall spectral spike that commutes from an initial positive frequency of around 250 Hz to a negative frequency of −250 Hz. This behavior is consistent with the theoretical models of electromagnetic wave propagation when the source and the observer are in motion [33], [34].

Figure 20 shows another segment of the spectrogram given in Fig. 15 during a second event involving a rapidly oncoming truck. However, this event took place on a curved stretch bordered on the right-hand side (from the test vehicles' perspective) by a long and tall hillside, and on the left-hand side by a short rocky wall. Figure 21 presents a sequence of pictures of the propagation scenario taken by the transmitter at different time instants during the event. The corresponding Doppler spectra recorded at such time instants are shown in Fig. 22. An important difference with the previous event is that the LOS path with the oncoming truck was obstructed for most of the event duration. First, an initial blockage between the transmitter and the truck was caused by the short rocky wall (see Fig. 21(a)). Then a subsequent blockage between this truck and the receiver was yielded by a second truck located right in front of the receiver (see Fig. 21(b)). Despite such blockages, a non-LOS (NLOS) link among the transmitter, the oncoming truck, and the receiver was presumably maintained at all times during the event by a double reflection mechanism. Note that the initial LOS obstruction between the transmitter and the oncoming truck can be circumvented if the probe signal is reflected either by the long hillside or by the second truck (cf. Fig. 21(a)). Then, the signal can be reflected once more by the oncoming truck in the direction of the receiver. This is plausible, as the LOS between the receiver and the oncoming truck was not blocked at the beginning of the event, since the road's curvature kept the second trailer (in front of the receiver) out

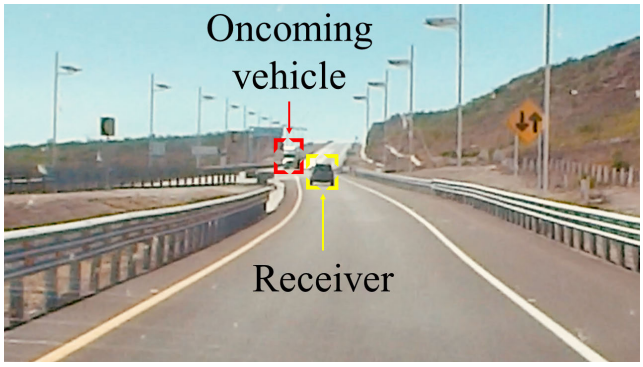

(a) Oncoming vehicle approaching the receiver (time instant $t_a = 112.8$ s)

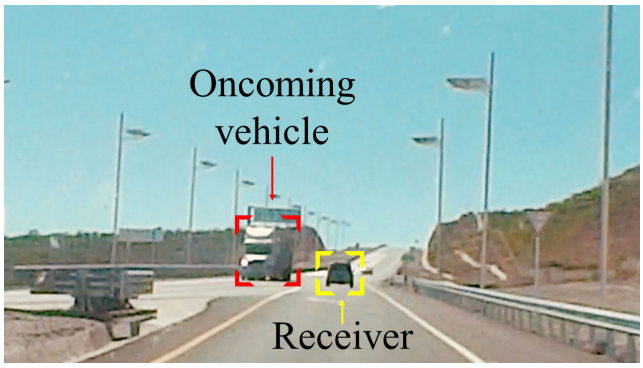

(b) Oncoming vehicle side-by-side wih the receiver (time instant $t_b = 115.8$ s)

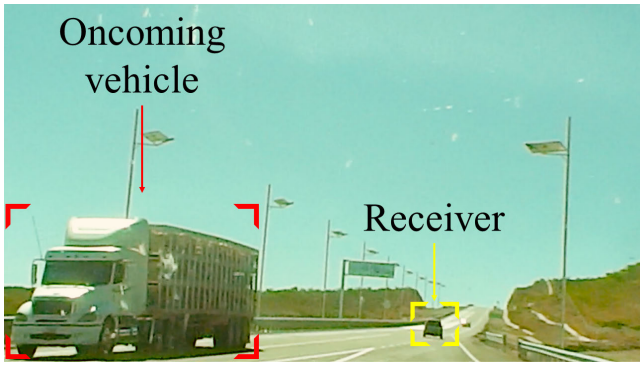

(c) Oncoming vehicle driving away from the receiver (time instant $t_c = 119.8$ s)

FIGURE 18. Photo sequence of an event in which a rapidly oncoming vehicle passes by the receiver in an open-field road section.

of the visual field. Such a doubly-reflected signal produces a spectral spike whose frequency would be Doppler shifted to a positive value exceeding the maximum Doppler shift, $\nu_{\max}^{sta}(t)$, caused by static reflectors. It occurs under the aforementioned conditions as the doubly-reflected signal's direction of arrival and the receiver's direction of motion are nearly the same. A spectral spike with such characteristics, located at a frequency of 270 Hz, was recorded at the beginning of the event, as observed in Fig. 22. The event becomes even more interesting when the LOS path between the receiver and the oncoming truck is obstructed by the second truck, whereas the transmitter has a LOS path to both the receiver and the

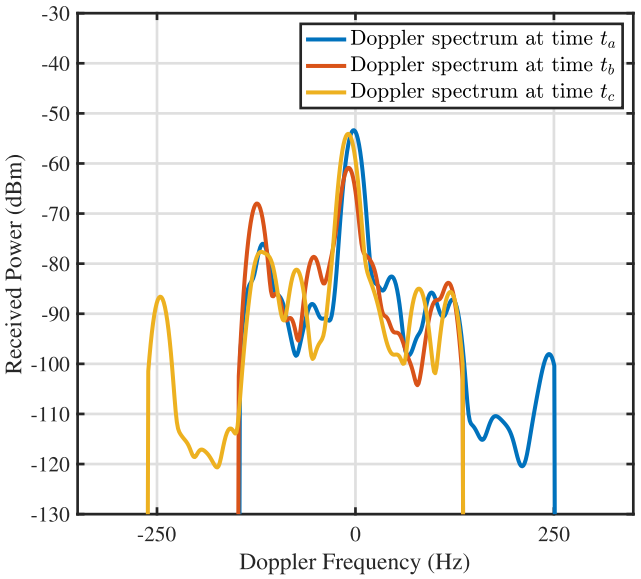

FIGURE 19. Doppler spectrum recorded at 760 MHz and three different time instants ($t_a = 112.8$ s, $t_b = 115.8$ s, $t_c = 119.8$ s) during an event involving a rapidly oncoming vehicle in an open-field road section.

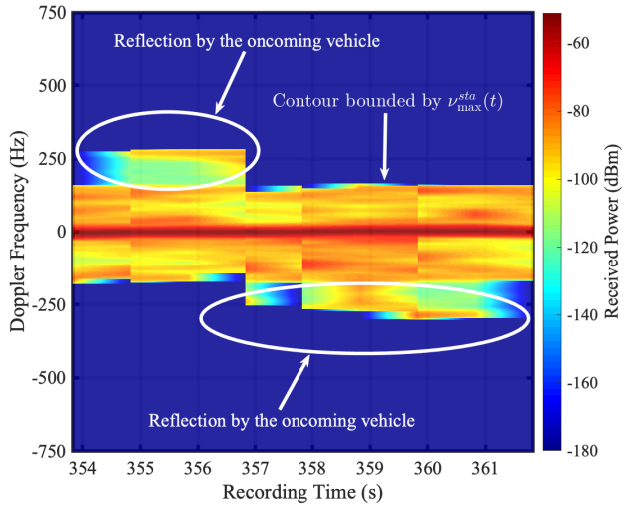

FIGURE 20. An interval of a pre-processed spectrogram recorded at 760 MHz during an event involving a rapidly oncoming vehicle in a curved road section.

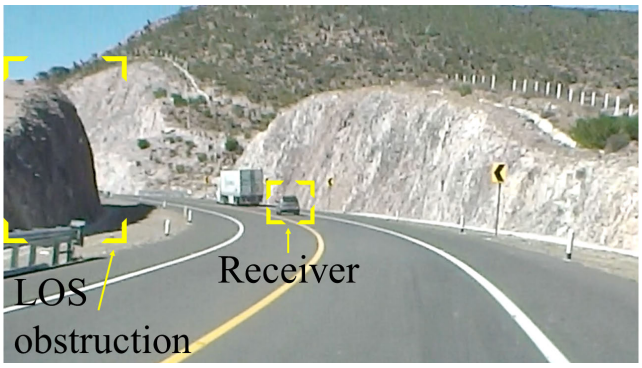

(a) Oncoming vehicle hidden to the transmitter by the rock wall on the left-hand side (time instant $t_d = 354.8$ s)

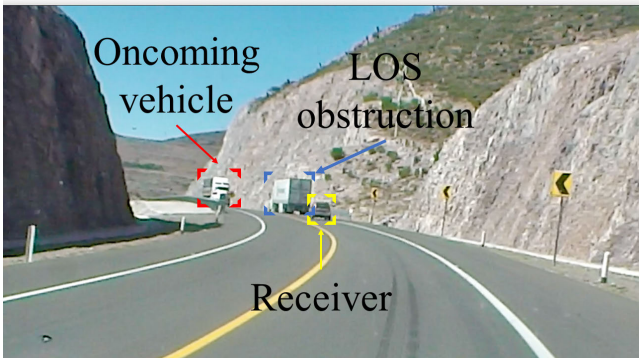

(b) Oncoming vehicle hidden to the receiver by a second truck (time instant $t_e = 357.8$ s)

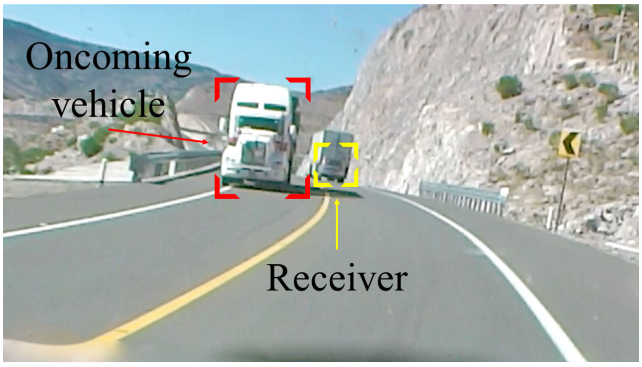

(c) Oncoming vehicle driving away from the receiver (time instant $t_f = 359.8$ s)

FIGURE 21. Photo sequence of an event in which a rapidly oncoming vehicle passes by the receiver in a curved road section.

oncoming truck, as illustrated in Fig. 21(b). The obstruction by the second truck hinders a direct reception of the signal reflected by the oncoming truck. However, the geometrical configuration of the propagation scenario allows the reflected signal to propagate back to the transmitter and undergo a second reflection off this latter vehicle in direction to the receiver. The resulting doubly-reflected signal will produce a spectral spike at a negative frequency smaller than $-\nu_{\max}^{sta}(t)$ because the signal's direction of arrival, and the receiver's direction of motion are nearly opposite in this case. This explains the spectral spikes at -260 and -280 Hz in Fig. 22.

Several events similar to the two analyzed above were recorded along the measurements route. These events, which involved even small vehicles, can be identified in Figs. 15 and 16 by the small white spots and vertical whiskers (lines) coming out of the contour bounded by $\nu_{\max}^{sta}(t)$.

Regarding the Doppler signatures of overtaking maneuvers, Fig. 23 shows a thirty-one seconds segment of a spectrogram recorded at 2,500 MHz in an open-field road scenario. This segment corresponds to the moments where the transmitter increased its velocity to approach the receiver, changed lanes, performed the overtaking, and reincorporated to its original lane. The maneuver was conducted in a coordinated manner using portable two-way radios and with

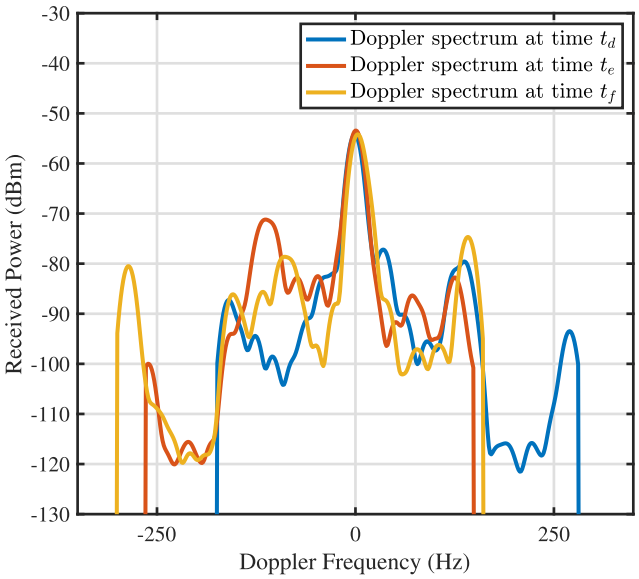

FIGURE 22. Doppler spectrum recorded at 760 MHz and three different time instants ($t_d = 354.8$ s, $t_e = 357.8$ s, $t_f = 359.8$ s) during an event involving a rapidly oncoming vehicle in a curved road section.

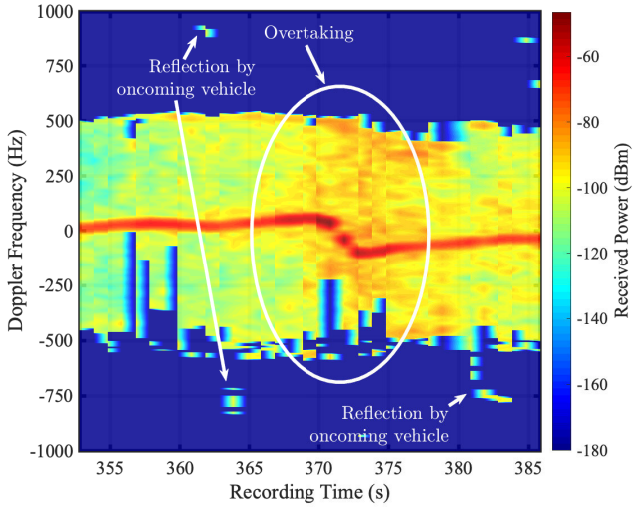

FIGURE 23. An interval of a pre-processed spectrogram recorded at 2,500 MHz during an overtaking maneuver.

the test vehicles having a LOS path to each other. At the beginning of the maneuver, and as a result of the transmitter's acceleration, the probe signal's frequency shifts slightly away from the origin toward positive frequencies. Then, as the transmitter passes by the receiver, the signal's frequency drifts rapidly to the negative frequencies. Finally, when the transmitter changes lanes again and decelerates to complete the maneuver, the probe signal's frequency drifts once again in direction to positive frequencies to relocate around the origin. A similar Doppler signature was observed when the transmitter was overtaken by the receiver.

C. DOPPLER STATISTICS

The spectral moments of the empirical instantaneous Doppler spectrum can also be computed from the data recorded during our experiments. Two important moments of the Doppler spectrum are the mean Doppler shift and the Doppler spread [59]. The mean Doppler shift describes the mean frequency drift that the signal experiences due to the relative motion between the transmitting and receiving vehicles. In turn, the Doppler spread describes the frequency spread that the signal experiences during the transmission. By considering the empirical Doppler spectrum $\tilde{S}(\nu, t'_k)$, the instantaneous mean Doppler shift can be computed as

$$B_1(t'_k) = \frac{\int_{-\infty}^{\infty} \nu \tilde{S}(\nu, t'_k)\, \mathrm{d}\nu}{\int_{-\infty}^{\infty} \tilde{S}(\nu, t'_k)\, \mathrm{d}\nu}. \tag{16}$$

The empirical instantaneous Doppler spread is given by

$$B_2(t'_k) = \sqrt{\frac{\int_{-\infty}^{\infty} \left(\nu - B_1(t'_k)\right)^2 \tilde{S}(\nu, t'_k)\, \mathrm{d}\nu}{\int_{-\infty}^{\infty} \tilde{S}(\nu, t'_k)\, \mathrm{d}\nu}}. \tag{17}$$

In practice, the range of measured frequencies does not extend to infinity. Therefore, we compute these statistics by integrating only over the measured frequency window.

In addition to the instantaneous values of $B_1(t'_k)$ and $B_2(t'_k)$, we also computed the empirical distributions of these two spectral moments and tested their fitting against several well-known theoretical distributions. The parameters of such theoretical distributions were obtained via maximum likelihood estimation using the `fitdist` function of MATLAB©. This function allows testing twenty-one different distributions. Nonetheless, for the analysis of $B_1(t'_k)$, we can only work with six distributions, as the other sixteen are not valid for continuous random variables, or their range is limited to positive values. However, for the analysis of $B_2(t'_k)$, we can test nineteen different continuous distributions. Furthermore, we conducted a goodness-of-fit test on each estimated theoretical distribution to determine whether a particular theoretical model is suitable for the measured data. Specifically, we considered the Kolgomorov-Smirnov goodness-of-fit (KSGOF) test at a significance level of 5%. In addition, we computed the Jensen-Shannon divergence (JSD) to determine which of the distributions that passed the test provide the best fit against the measured data.

1) MEAN DOPPLER SHIFT

We first analyze the mean Doppler shift of the spectrograms presented in Figs. 15 and 16. The waveform of $B_1(t'_k)$ computed at 760 MHz is shown in Fig. 24. For this particular waveform, the time-averaged mean Doppler shift,

$$\overline{B}_1 = \frac{1}{K} \sum_{k=1}^{K} B_1(t'_k) \tag{18}$$

is equal to $\overline{B}_1 = -5.13$ Hz, whereas the standard deviation of $B_1(t'_k)$

$$\overline{\sigma}_1 = \sqrt{\frac{1}{K} \sum_{k=1}^{K} [B_1(t'_k) - \overline{B}_1]^2} \tag{19}$$

is equal to $\overline{\sigma}_1 = 10.72$ Hz. From Fig. 24, we can observe that the mean Doppler shift fluctuates slightly around the

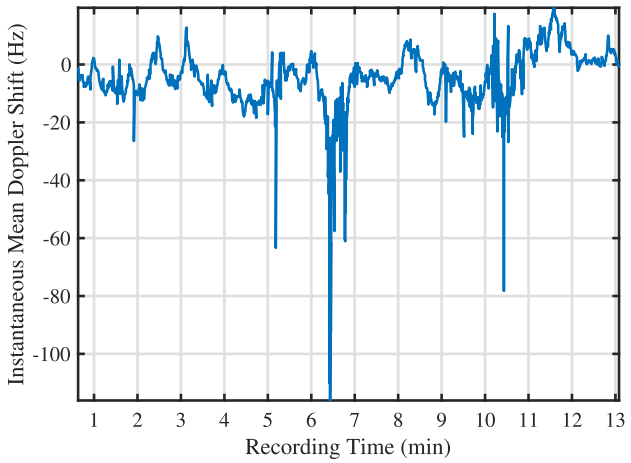

FIGURE 24. Instantaneous mean Doppler shift of a measured spectrogram at 760 MHz.

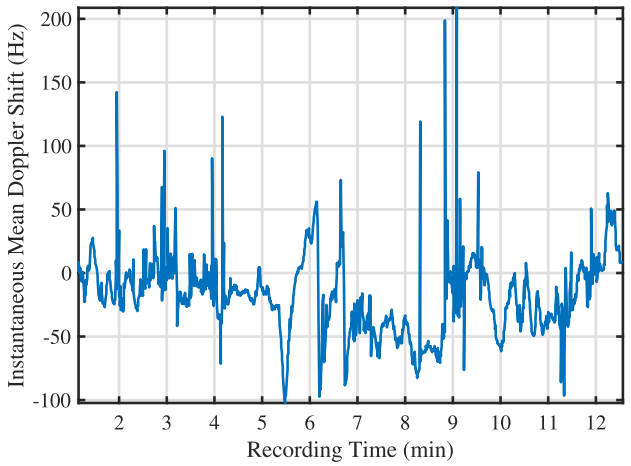

FIGURE 25. Instantaneous mean Doppler shift of a measured spectrogram 2,500 MHz.

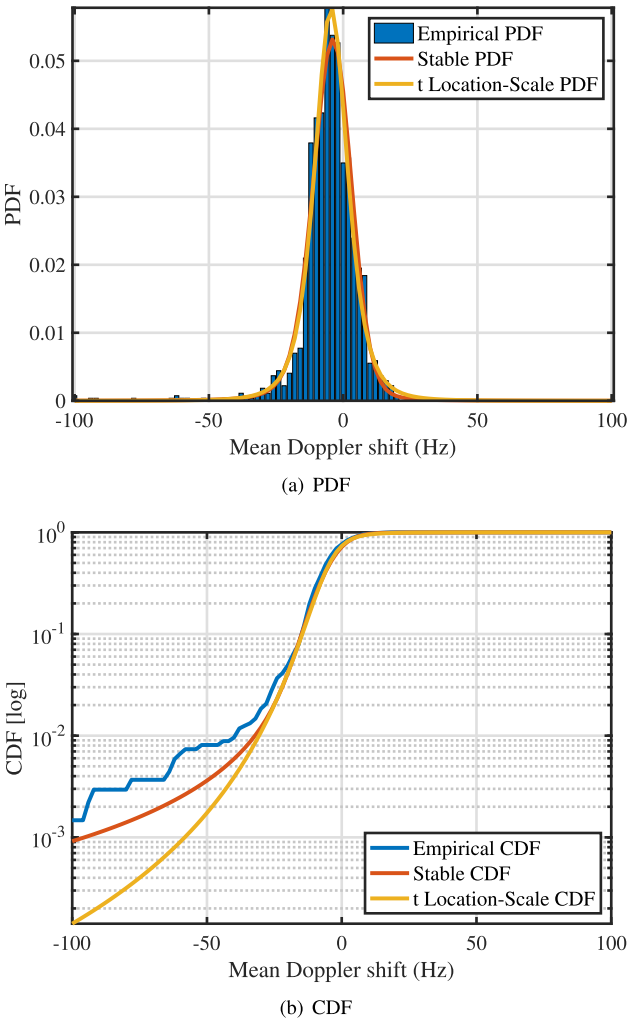

FIGURE 26. Empirical distribution of the instantaneous mean Doppler shift at 760 MHz.

central frequency, but it has sharp peak values of up to −60, −80, and −116 Hz. The videos recorded over the route reveal that these peak values correspond to scenarios in which the transmitter was left behind by a rapidly accelerating receiver. In fact, the largest values at −80 and −116 Hz were recorded under NLOS conditions. On the other hand, Fig. 25 shows the waveform of $B_1(t_k')$ computed from the spectrogram at 2,500 MHz. For this waveform, we have $\overline{B}_1 = -18.19$ Hz and $\overline{\sigma}_1 = 31.0729$ Hz. The largest peak value of $B_1(t_k')$, which is of about 205 Hz and can be observed in Fig. 25 at $t \approx 9$ min, was caused by an accelerating transmitter in a maneuver to shorten the distance to the receiver.

The empirical probability distribution function (PDF) and cumulative distribution function (CDF) of $B_1(t_k')$, computed from the spectrogram recorded at 760 MHz, are presented in Fig. 26. The theoretical distributions that passed the KSGOF test, namely the Stable and t Location-Scale distributions, are also shown in Fig. 26. The JSD was equal to 0.0100 and 0.0103, for the Stable and t Location-Scale distributions, respectively. Based on this metric, we conclude that the best fitting is obtained for the Stable distribution with parameters $\alpha = 1.76$, $\beta = -0.37$, $\gamma = 5.32$, and $\delta = -3.99$.

Likewise, the empirical distribution of the instantaneous mean Doppler shift at 2,500 MHz is shown in Fig. 27. We observe that the mean Doppler shift spreads over a larger range of values. This occurs because the Doppler shift is larger as the carrier frequency increases. Moreover, the values are distributed around the proximity of the central frequency. The Logistic and t Location-Scale distributions were the models that passed the KSGOF test and their corresponding JSD was equal to 0.0133 and 0.0128, respectively. Based on the JSD, it follows that the t Location-Scale distribution provides the best fitting. For this distribution, the estimated parameters are equal to $\mu = -18.64$, $\sigma = 24.32$, $\nu = 5.42$.

The empirical and theoretical distributions of $B_1(t_k')$ presented in Figs. 26 and 27 show that the measured instantaneous mean Doppler shift is distributed almost symmetrically around its average value, $\overline{B}_1$. This observation is consistent with the geometry of the three propagation scenarios described in Section IV. Moreover, the fact that the

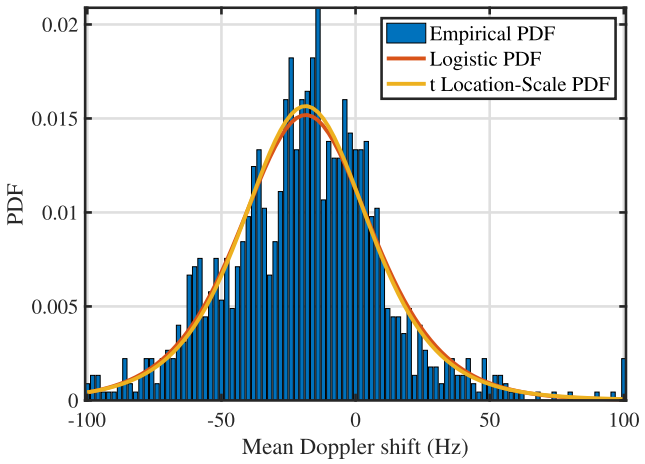

(a) PDF

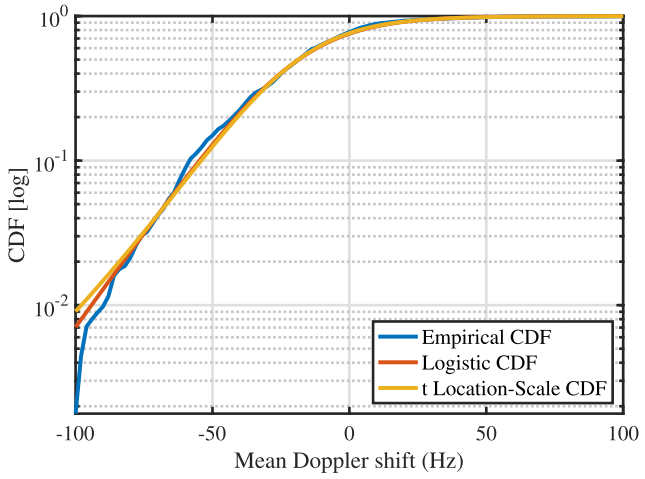

(b) CDF

FIGURE 27. Empirical distribution of the instantaneous mean Doppler shift at 2,500 MHz.

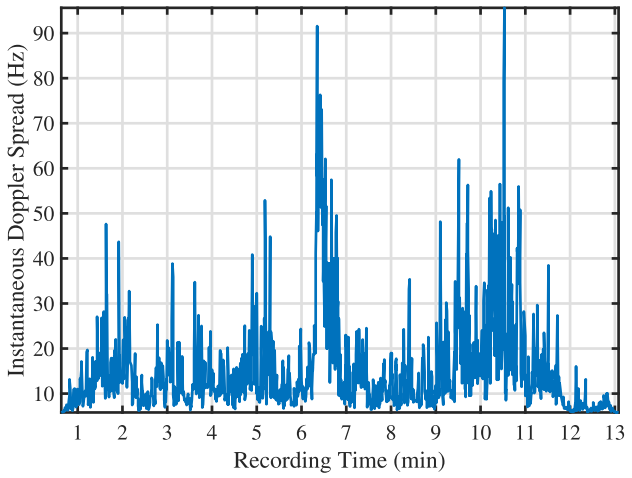

FIGURE 28. Instantaneous Doppler spread of a measured spectrogram at 760 MHz.

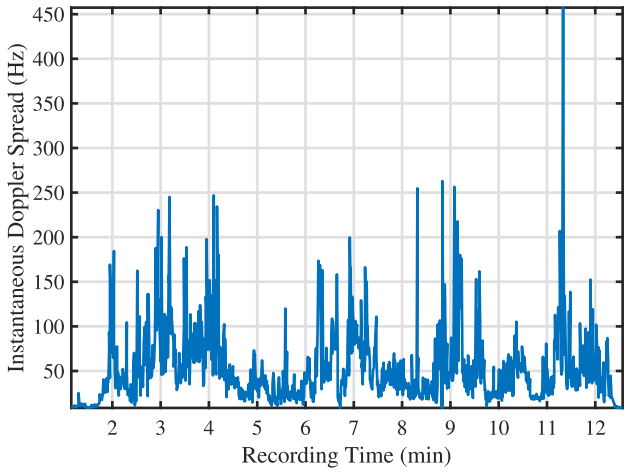

FIGURE 29. Instantaneous Doppler spread of a measured spectrogram at 2,500 MHz.

time-averaged value of $B_1(t'_k)$ is negative for the two carrier frequencies suggests that the multipath signal was arriving at the receiver mainly from a direction opposite to the direction of motion of this vehicle. This is also consistent with how the experiments were carried out. Hence, the obtained results indicate that our measurement platform provides coherent information about the statistics of $B_1(t'_k)$.

2) DOPPLER SPREAD

We next analyze the Doppler spread of the pre-processed spectrograms in Figs. 15 and 16. The instantaneous Doppler spread, $B_2(t'_k)$, computed from the spectrogram at 760 MHz is shown in Fig. 28, whereas the waveform of $B_2(t'_k)$ computed from the spectrogram at 2,500 MHz is presented in Fig. 29. Both figures show that the smallest values recorded for this spectral moment are not equal to zero. This occurs because the transmitted probe signal is not a perfect impulse function, as shown in Fig. 7. Therefore, the received power is not concentrated at a single frequency. Instead, it is distributed over a narrow bandwidth, causing a small bias in the computation of $B_2(t'_k)$. However, such a bias can be compensated easily. The behavior of the Doppler spread at 2,500 MHz is similar to the one observed at 760 MHz. Nonetheless, larger Doppler spread values are obtained at 2,500 MHz due to the larger spectral dispersion that results from increasing the carrier frequency. The effects of the carrier frequency on the Doppler spread are highlighted by the analysis of the time-averaged Doppler spread

$$\overline{B}_2 = \frac{1}{K}\sum_{k=1}^{K} B_2(t'_k) \tag{20}$$

and the standard deviation of $B_2(t'_k)$

$$\overline{\sigma}_2 = \sqrt{\frac{1}{K}\sum_{k=1}^{K}[B_2(t'_k) - \overline{B}_2]^2}. \tag{21}$$

For the waveform of $B_2(t'_k)$ at 760 MHz, we have $\overline{B}_2 = 15.84$ and $\overline{\sigma}_2 = 11.35$, whereas $\overline{B}_2 = 52.21$ and $\overline{\sigma}_2 = 40.3754$ for the waveform at 2, 500 MHz.

Regarding the distribution of $B_2(t'_k)$, Figs. 30 and 31 show curves of the empirical PDFs and CDFs of the waveforms presented in Figs. 28 and 29. For the probe signal at 760 MHz,

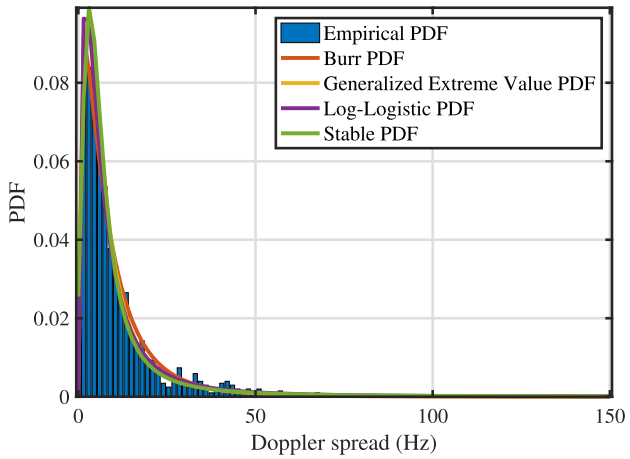

(a) PDF

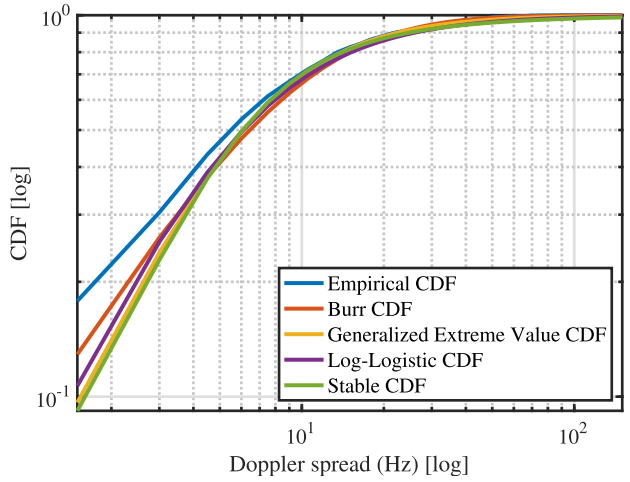

(b) CDF

FIGURE 30. Empirical distribution of the instantaneous Doppler spread at 760 MHz.

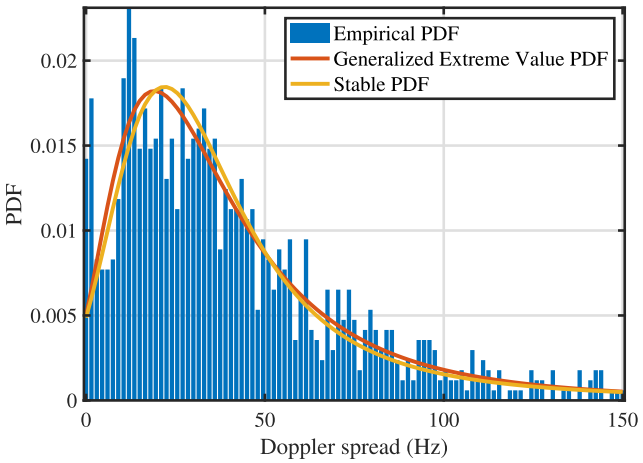

(a) PDF

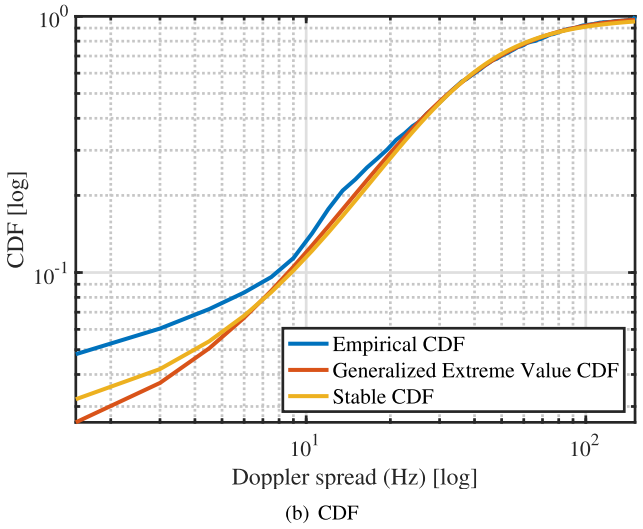

(b) CDF

FIGURE 31. Empirical distribution of the instantaneous Doppler spread at 2,500 MHz.

the empirical distribution of $B_2(t_k')$ can be fitted against the Burr, the Generalized Extreme Value, the Log-Logistic, and the Stable distributions, as these four theoretical distributions passed the KSGOF test. In that same order, the obtained JSD was equal to 0.0065, 0.0050, 0.0043, 0.0055. The best fitting was therefore against the Log-Logistic distribution with parameters $\mu = 1.80$ and $\sigma = 0.6594$. On the other hand, for the probe signal at 2, 500 MHz, the empirical distribution of $B_2(t_k')$ can be fitted only against the Generalized Extreme Value and the Stable distributions. The JSD of these two distributions was equal to 0.0167 and 0.0180, respectively, meaning that the best fitting was against the Generalized Extreme Value distribution. The estimated parameters of this distribution were $k = 0.28$, $\sigma = 20.97$ and $\mu = 24.18$.

The statistical results presented in Figs. 26, 27, 30 and 31 demonstrate that our measurement platform is an effective tool for the empirical characterization of the Doppler spectrum of V2V channels. However, such results are site specific, as they were obtained without considering the differences between the variety of propagation scenarios along the measurements route. To provide results that are meaningful beyond the particular location of our measurement experiments, we present in Table 3 the empirical statistics of $B_1(t_k')$ and $B_2(t_k')$ by considering a classification of propagation scenarios. Specifically, the classification is based on the three propagation scenarios described in SectionV-B. The results in Table 3 can be used as guidelines for the spectral moments analysis of V2V channels in highway scenarios having characteristics similar to those described in SectionV-B.

VII. PATH-LOSS AND LARGE-SCALE FADING

The measurement set up described in Section IV is commonly used to characterize the path-loss profile and large-scale fading distribution. In this section, we address the computation of these two statistics from the recorded Doppler spectrograms. Our analysis begins by decoupling the total received power into its path-loss and fading components.

TABLE 3. Statistics of the mean Doppler shift (MDS) and Doppler spread (DS) for the two carrier frequencies and the three scenarios described in SectionV-B.

Scenario	$\overline{B}_1$	$\overline{\sigma}_1$	$\overline{B}_2$	$\overline{\sigma}_2$	MDS PDF	MDS PDF Parameters	DS PDF	DS PDF Parameters
#1 @760 MHz	-7.44	11.17	17.35	12.97	Stable	$\alpha = 1.67, \beta = -0.63, \gamma = 4.60, \delta = -5.49$	Log-Logistic	$\mu = 1.85, \sigma = 0.67$
#2 @760 MHz	-7.86	9.68	15.65	9.11	Stable	$\alpha = 1.63, \beta = -0.99, \gamma = 3.98, \delta = -5.31$	Generalized Extreme Value	$k = 0.34, \sigma = 4.64, \mu = -0.22$
#3 @760 MHz	-0.64	8.94	13.77	9.36	Stable	$\alpha = 1.95, \beta = -0.99, \gamma = 5.75, \delta = -5.49$	Stable	$\alpha = 0.99, \beta = 0.99, \gamma = 2.46, \delta = 3.41$
#1 @2,500 MHz	-21.76	29.43	58.95	39.44	Logistic	$\mu = -22.02, \sigma = 15.23$	Log-Logistic	$\mu = 3.65, \sigma = 0.49$
#2 @2,500 MHz	-21.48	37.63	49.10	37.52	Generalized Extreme Value	$k = -0.12, \sigma = 33.11, \mu = -37.19$	Log-Logistic	$\mu = 3.34, \sigma = 0.65$
#3 @2,500 MHz	-12.64	29.73	45.10	41.18	t Location-Scale	$\mu = -12.37, \sigma = 19.09, \nu = 2.97$	Exponential	$\mu = 36.51$

By neglecting the power of the additive noise,[1] the instantaneous total received power in decibels (dB) of the Doppler spectrum $\tilde{S}(\nu, t'_k)$ is given by

$$\mathcal{P}(t'_k) = 10 \log_{10} \left(\int_{-\infty}^{\infty} \tilde{S}(\nu, t'_k) \, \mathrm{d}\nu \right). \tag{22}$$

In practice, the integration is computed only over the range of measured frequencies. The total received power can be separated into the contributions of the average power and the small-scale fading

$$\mathcal{P}(t'_k) = \mathcal{P}_{\mathrm{a}}(t'_k) + \mathcal{P}_{\mathrm{s}}(t'_k) \tag{23}$$

where $\mathcal{P}_{\mathrm{a}}(t'_k)$ is the average received power (in dB) and $\mathcal{P}_{\mathrm{s}}(t'_k)$ is the power of the small-scale fading (also in dB). The average power is computed here using a window filter over multiple observations of the total received power. The window filter vanishes the fluctuations of the total received power due to small-scale fading. In turn, the average received power is decoupled into two components as

$$\mathcal{P}_{\mathrm{a}}(t'_k) = \mathcal{P}_{\mathrm{d}}(t'_k) + \mathcal{P}_{\mathrm{l}}(t'_k) \tag{24}$$

where $\mathcal{P}_{\mathrm{d}}(t'_k)$ is the received power level due to path-loss effects given as a function of the distance, and $\mathcal{P}_{\mathrm{l}}(t'_k)$ are the contributions of the large-scale fading. The path-loss profile can be described by the linear function

$$\mathcal{P}_{\mathrm{d}}(t'_k) = \mathcal{P}_0 - Kd(t'_k) \tag{25}$$

where $\mathcal{P}_0$ is a reference power level, K is a constant related to the signal loss and $d(t'_k)$ is the instantaneous separation distance between vehicles at time t'_k.

To obtain the power statistics, we compute the instantaneous separation distance among the transmitting and receiving vehicles and decouple the corresponding power levels following (23)-(25). First, the instantaneous separation distances between vehicles are computed from the measured latitudes and longitudes using the haversine formula. Next, we compute the average received power by means of a window filter and perform linear regression to obtain the empirical path-loss profile. Finally, we compute the empirical distributions of the large-scale fading. The empirical distributions of the fading statistics were computed harnessing all the experimental data measured at the corresponding frequencies. We fit the empirical fading distributions to theoretical PDFs. For our experiments, the best fitting was obtained against the log-normal distribution for the empirical large-scale fading.

The proper identification of the availability of LOS conditions in the measured intervals is obtained by inspecting the recorded videos synced with the time information of the measured spectrograms. The visualization of the instantaneous power measures and the availability of LOS conditions enables us to observe and understand the effects of attenuation due to the separation distance and fading, as well as the repercussions of losing the LOS paths.

The instantaneous received power during a time interval of a measured spectrogram at 760 MHz is depicted in Fig. 32. We plotted the total received power, the average received power and the indicator of the availability of LOS conditions. The empirical data were obtained for the pre-processed spectrogram in Fig. 15. The total received power presents multiple fluctuations due to small-scale fading. The average received power has a more uniform behavior since the vehicles' motion profiles were almost constant during the observed time interval. However, the unavailability of LOS conditions paired with the separation distance among vehicles produce losses in the average received power, e.g., in the interval from 190 to 210 s.

Figure 33 shows the received power during an interval of a measured spectrogram at 2,500 MHz. This figure presents curves of the total received power, the average received power, and the indicator of the availability of LOS conditions corresponding to the spectrogram in Fig. 16. In this particular interval, the LOS conditions were available in most observations. In this spectrogram segment, the transmitting and receiving vehicles were accelerating to increase their speeds and separation distance. Indeed, this effect is observed during the first 70 s of the interval, where the received power

[1]This consideration is justified since we apply a noise floor threshold to the measured spectrograms in the pre-processing stage.

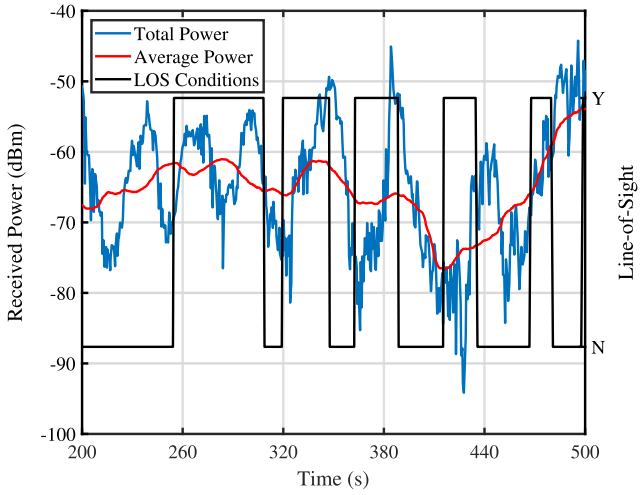

FIGURE 32. Received power of a measured spectrogram at 760 MHz.

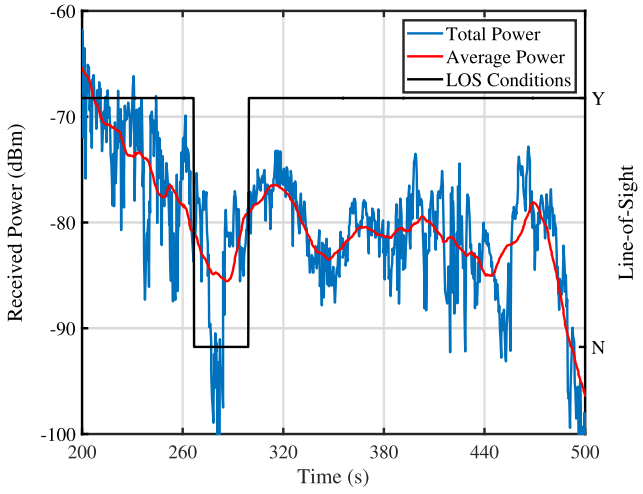

FIGURE 33. Received power of a measured spectrogram at 2,500 MHz.

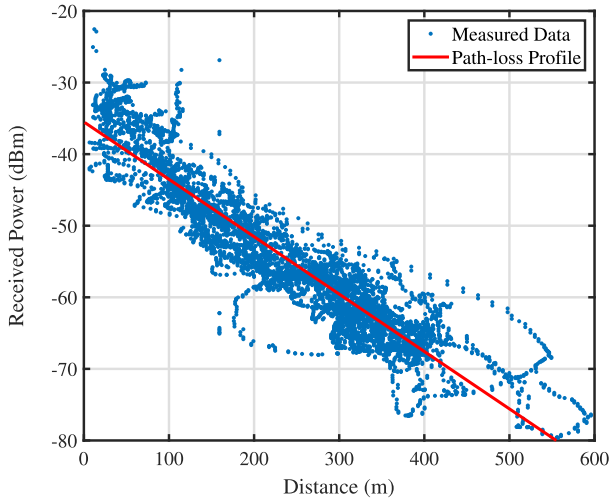

FIGURE 34. Empirical path-loss profile at 760 MHz.

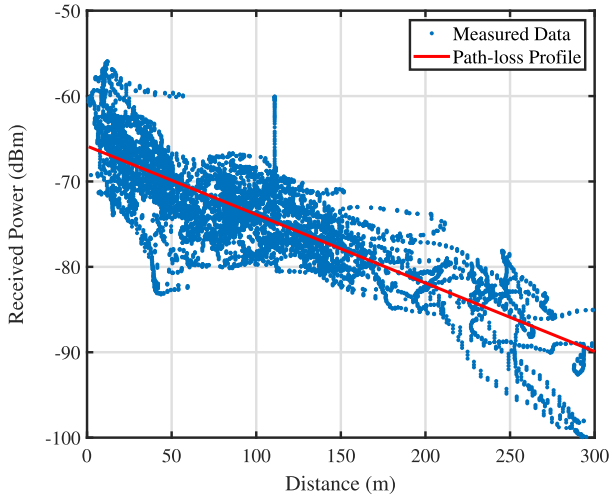

FIGURE 35. Empirical path-loss profile at 2,500 MHz.

decays over time as the vehicles separate. A second power decay is shown at the end of this interval, in which the separation distance among vehicles increases and the signal attenuates. Moreover, we can observe the effects of losing the LOS conditions in the interval from 70 to 90 s, where the signal experiences a severe attenuation.

A. PATH-LOSS

We first focus our attention on the empirical path-loss profiles of the measured data at 760 MHz and 2,500 MHz. The empirical path-loss profile of the measured spectrograms at 760 MHz is depicted in Fig. 34. This plot shows the constellation of the measured data and the linear function that describes the path-loss profile. The constellation of measured data shows that most experiments were performed with separation distances between 100 and 400 m. The obtained parameters for this empirical path-loss profile are $P_0 = -35.50$ dBm and $K = 0.08$. Moreover, Fig. 35 shows the empirical path-loss profile of the measured spectrograms at 2,500 MHz. The separation distances of the experiments performed at 2,500 MHz were mainly between 50 and 150 m. The corresponding parameters for the empirical path-loss profile at 2,500 MHz are $P_0 = -65.85$ dBm and $K = 0.08$. These results show that the path-loss profile varies with the carrier frequency. Indeed, the losses at a higher frequency are more significant, as can be observed in the spectrograms shown in Figs. 15 and 16.

B. LARGE-SCALE FADING

We next analyze the empirical distributions of the power of large-scale fading for both measured carrier frequencies at 760 MHz and 2,500 MHz. The empirical distribution of the large-scale fading at 760 MHz is depicted in Fig. 36. The empirical distribution was fitted against a log-normal distribution with $\mu = 0$ and $\sigma = 0.89$. The theoretical PDF has a shape similar to the empirical distribution and fits well the data for most power levels. Furthermore, Fig. 37

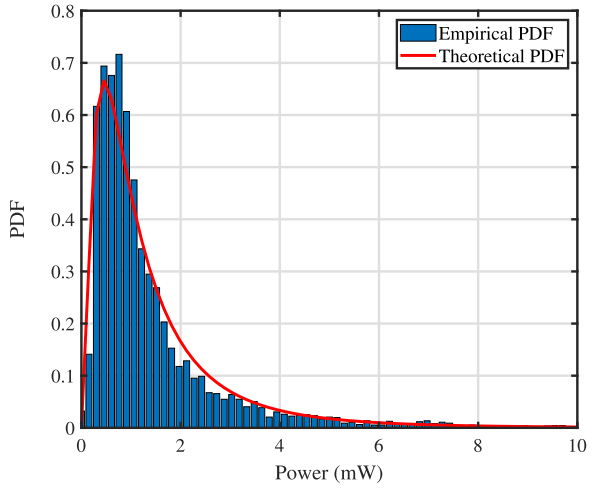

FIGURE 36. Empirical large-scale fading distribution at 760 MHz.

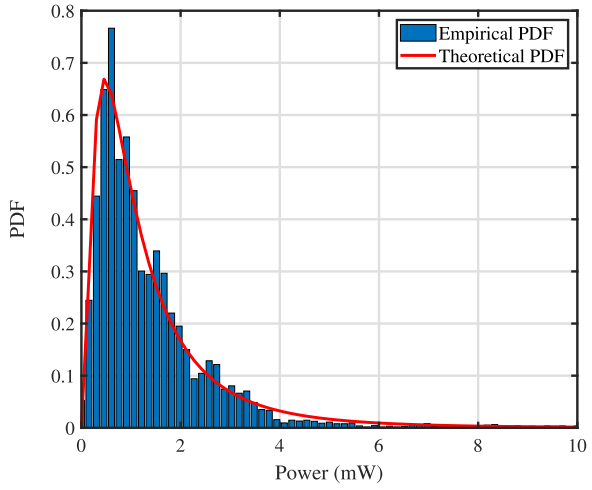

FIGURE 37. Empirical large-scale fading distribution at 2,500 MHz.

shows the empirical distribution of the large-scale fading for the carrier frequency at 2,500 MHz. This empirical result is similar to the one obtained for the measurements at 760 MHz with small differences in the tail of the distribution. The theoretical PDF fitted to the latter empirical data follows a log-normal distribution with $\mu = 0$ and $\sigma = 0.87$, which verify the similarity between both empirical distributions.

VIII. FINAL REMARKS

In this paper, we described the implementation of a Doppler spectrum measurement platform for time-varying V2V channels that can be assembled using general-purpose hardware. This platform employs an RF signal generator and an SA to record traces of the channel's Doppler spectrum. Similar platforms have been widely employed to gather empirical data of the channel's path-loss profile and fading statistics. However, we have shown here that the same channel sounding architecture can be harnessed as well to measure the channel's time-varying Doppler spectrum.

We assessed the capabilities of our implementation by performing field experiments at 760 MHz and 2,500 MHz in highway scenarios near San Luis Potosí, México. The obtained results demonstrate that our measurement platform lends itself for the empirical characterization of the channel's time-varying spectral moments. The results also show that our platform allows to identify the Doppler signatures of the V2V channel during events relevant to road safety. In fact, the spectral signature of one of the events analyzed in this paper shows that the transmitted signal may reach the receiver by a double-reflection mechanism. While this propagation mechanism has been previously reported and modeled in the literature, the results presented here suggest that the body of the transmitting vehicle can also be involved in such a double reflection path. To the best of the authors' knowledge, the role of the transmitter (and by extension, of the receiver) as a potential reflector has not been considered for the modeling of double-reflection (or double-scattering) multipath V2V channels.

We also analyzed the empirical statistics of the instantaneous mean Doppler shift and Doppler spread for three different propagation scenarios that are commonly found on a mountainous road, namely: A scenario with rock walls on both sides of the road, a scenario with rock walls only on one side of the road, and an open field road. The mean Doppler shifts were distributed almost symmetrically around their average value. The largest Doppler spread was observed in the former scenario (two rock walls), whereas the smallest was observed in the latter (open field), as one would expect. In addition, we computed the empirical path-loss profile and the empirical distributions of the large-scale fading. The path-loss profile of our measured data was modeled by a linear function, whereas the empirical distribution of the large-scale fading provided a good fitting against the log-normal PDF.

ACKNOWLEDGMENT

The authors would like to thank Dr. María del Socorro Ruiz Rodríguez, Former Director of the Students Services Division, Universidad Autonóma de San Luis Potosi, Miguel Aarón Gutiérrez Díaz de León, and Jesús Omar Contreras Ponce, for the loan of the vehicles that were used as test vehicles during the measurement campaign. Additional thanks are due to Mariana Lara Alfaro and Jesús Omar Contreras Ponce for their valuable assistance with the instrumentation and development of the measurement experiments. The authors are also grateful to the Associate Editor, Dr. Hassan Omar, and the anonymous reviewers, for their helpful comments and constructive criticism.

REFERENCES

[1] P. Papadimitratos, A. De La Fortelle, K. Evenssen, R. Brignolo, and S. Cosenza, "Vehicular communication systems: Enabling technologies, applications, and future outlook on intelligent transportation," *IEEE Commun. Mag.*, vol. 47, no. 11, pp. 84–95, Nov. 2009.

[2] G. Dimitrakopoulos and P. Demestichas, "Intelligent transportation systems," *IEEE Veh. Technol. Mag.*, vol. 5, no. 1, pp. 77–84, Mar. 2010.

[3] J. B. Kenney, "Dedicated short-range communications (DSRC) standards in the United States," *Proc. IEEE*, vol. 99, no. 7, pp. 1162–1182, Jul. 2011.

[4] G. Karagiannis, O. Altintas, E. Ekici, G. Heijenk, B. Jarupan, K. Lin, and T. Weil, "Vehicular networking: A survey and tutorial on requirements, architectures, challenges, standards and solutions," *IEEE Commun. Surveys Tuts.*, vol. 13, no. 4, pp. 584–616, Nov. 2011.

[5] G. Rafiq, B. Talha, M. Patzold, J. G. Luis, G. Ripa, I. Carreras, C. Coviello, S. Marzorati, G. P. Rodriguez, G. Herrero, and M. Desaeger, "What's new in intelligent transportation systems?: An overview of European projects and initiatives," *IEEE Veh. Technol. Mag.*, vol. 8, no. 4, pp. 45–69, Dec. 2013.

[6] T. G. McGiffen, S. Beiker, and A. Paulraj, "Motivating network deployment: Vehicular communications," *IEEE Veh. Technol. Mag.*, vol. 12, no. 3, pp. 22–33, Sep. 2017.

[7] G. Naik, B. Choudhury, and J.-M. Park, "IEEE 802.11 bd & 5G NR V2X: Evolution of radio access technologies for V2X communications," *IEEE Access*, vol. 7, pp. 70169–70184, 2019.

[8] Z. H. Mir, J. Toutouh, F. Filali, and Y.-B. Ko, "Enabling DSRC and C-V2X integrated hybrid vehicular networks: Architecture and protocol," *IEEE Access*, vol. 8, pp. 180909–180927, 2020.

[9] *IEEE Standard for Information Technology–Telecommunications and Information Exchange Between Systems—Local and Metropolitan Area Networks–Specific Requirements—Part 11: Wireless LAN Medium Access Control (MAC) and Physical Layer (PHY) Specifications*, IEEE Standard 802.11-2020, 2021.

[10] *700 MHz Band Intelligent Transport Systems*, Standard ARIB STD-T109, 2013.

[11] H. Seo, K.-D. Lee, S. Yasukawa, Y. Peng, and P. Sartori, "LTE evolution for vehicle-to-everything services," *IEEE Commun. Mag.*, vol. 54, no. 6, pp. 22–28, Jun. 2016.

[12] S. Chen, J. Hu, Y. Shi, Y. Peng, J. Fang, R. Zhao, and L. Zhao, "Vehicle-to-everything (V2X) services supported by LTE-based systems and 5G," *IEEE Commun. Standards Mag.*, vol. 1, no. 2, pp. 70–76, Jun. 2017.

[13] *3rd Generation Partnership Project; Technical Specification Group Services and System Aspects; Release 14 Description; Summary of Rel-14 Work Items (Release 14)*, 3GPP, document TR 21.914 V14.0.0 (2018-05), 2018.

[14] *3rd Generation Partnership Project; Technical Specification Group Services and System Aspects; Release 16 Description; Summary of Rel-16 Work Items (Release 16)*, 3GPP, document TR 21.916 V0.4.0 (2020-03), 2019.

[15] J. Gozalvez, M. Sepulcre, and R. Bauza, "Impact of the radio channel modelling on the performance of VANET communication protocols," *Telecommun. Syst.*, vol. 50, no. 3, pp. 149–167, Jul. 2012.

[16] C. F. Mecklenbrauker, A. Molisch, J. Karedal, F. Tufvesson, A. Paier, L. Bernadó, T. Zemen, O. Klemp, and N. Czink, "Vehicular channel characterization and its implications for wireless system design and performance," *Proc. IEEE*, vol. 99, no. 7, pp. 1189–1212, Jul. 2011.

[17] J. A. Fernandez, K. Borries, L. Cheng, B. V. K. V. Kumar, D. D. Stancil, and F. Bai, "Performance of the 802.11 p physical layer in vehicle-to-vehicle environments," *IEEE Trans. Veh. Technol.*, vol. 61, no. 1, pp. 3–14, Jan. 2012.

[18] Y. M. Khattabi and M. M. Matalgah, "Alamouti-OSTBC wireless cooperative networks with mobile nodes and imperfect CSI estimation," *IEEE Trans. Veh. Technol.*, vol. 67, no. 4, pp. 3447–3456, Apr. 2018.

[19] L. Hu, H. Wang, and Y. Zhao, "Performance analysis of DSRC-based vehicular safety communication in imperfect channels," *IEEE Access*, vol. 8, pp. 107399–107408, 2020.

[20] S. Yadav and A. Pandey, "Secrecy performance of cognitive vehicular radio networks: Joint impact of nodes mobility and imperfect channel estimates," in *Proc. IEEE Int. Black Sea Conf. Commun. Netw. (BlackSeaCom)*, May 2020, pp. 1–7.

[21] J. J. Jaime-Rodríguez, C. A. Gómez-Vega, C. A. Gutiérrez, J. M. Luna-Rivera, D. U. Campos-Delgado, and R. Velázque, "A non-WSSUS channel simulator for V2X communication systems," *Electronics*, vol. 9, no. 8, pp. 1–25, 2020.

[22] S. Bolufé, C. A. Azurdia-Meza, S. Céspedes, S. Montejo-Sánchez, R. D. Souza, and E. M. G. Fernandez, "POSACC: Position-accuracy based adaptive beaconing algorithm for cooperative vehicular safety systems," *IEEE Access*, vol. 8, pp. 15484–15501, 2020.

[23] E. Meesa-ard and S. Pattaramalai, "Evaluating the mobility impact on the performance of heterogeneous wireless networks over η–μ fading channels," *IEEE Access*, vol. 9, pp. 65017–65032, 2021.

[24] Y. Alghorani, G. Kaddoum, S. Muhaidat, S. Pierre, and N. Al-Dhahir, "On the performance of multihop-intervehicular communications systems over *n**Rayleigh fading channels," *IEEE Wireless Commun. Lett.*, vol. 5, no. 2, pp. 116–119, Apr. 2016.

[25] C. A. Gutiérrez, J. J. Jaime-Rodríguez, J. M. Luna-Rivera, D. U. Campos-Delgado, and J. Vázquez Castillo, "Modeling of non-WSSUS double-Rayleigh fading channels for vehicular communications," *Wireless Commun. Mobile Comput.*, vol. 2017, pp. 1–15, Oct. 2017.

[26] A. Pandey and S. Yadav, "Joint impact of nodes mobility and imperfect channel estimates on the secrecy performance of cognitive radio vehicular networks over Nakagami-*m* fading channels," *IEEE Open J. Veh. Technol.*, vol. 2, pp. 289–309, 2021.

[27] P. Almers, E. Bonek, A. Burr, N. Czink, M. Debbah, V. Degli-Esposti, H. Hofstetter, P. Kyösti, D. Laurenson, G. Matz, A. F. Molisch, C. Oestges, and H. Özcelik, "Survey of channel and radio propagation models for wireless MIMO systems," *EURASIP J. Wireless Commun. Netw.*, vol. 2007, no. 1, pp. 1–19, Feb. 2007.

[28] D. W. Matolak, "Modeling the vehicle-to-vehicle propagation channel: A review," *Radio Sci.*, vol. 49, no. 9, pp. 721–736, Sep. 2014.

[29] M. Boban, J. Barros, and O. K. Tonguz, "Geometry-based vehicle-to-vehicle channel modeling for large-scale simulation," *IEEE Trans. Veh. Technol.*, vol. 63, no. 9, pp. 4146–4164, Nov. 2014.

[30] A. F. Molisch, F. Tufvesson, J. Kåredal, and C. F. Mecklenbräuker, "A survey on vehicle-to-vehicle propagation channels," *IEEE Commun. Mag.*, vol. 16, no. 6, pp. 12–22, Dec. 2009.

[31] Y. Ma, L. Yang, and X. Zheng, "A geometry-based non-stationary MIMO channel model for vehicular communications," *China Commun.*, vol. 15, no. 7, pp. 30–38, Jul. 2018.

[32] C. A. Gutiérrez, J. T. Gutiérrez-Mena, J. M. Luna-Rivera, D. U. Campos-Delgado, R. Velázquez, and M. Pätzold, "Geometry-based statistical modeling of non-WSSUS mobile-to-mobile Rayleigh fading channels," *IEEE Trans. Veh. Technol.*, vol. 67, no. 1, pp. 362–377, Jan. 2018.

[33] W. Dahech and M. Pätzold, C. A. Gutiérrez, and N. Youssef, "A non-stationary mobile-to-mobile channel model allowing for velocity and trajectory variations of the mobile stations," *IEEE Trans. Wireless Commun.*, vol. 16, no. 3, pp. 1987–2000, Mar. 2017.

[34] K. Jiang, X. Chen, Q. Zhu, L. Chen, D. Xu, and B. Chen, "A novel simulation model for nonstationary Rice fading channels," *Wireless Commun. Mobile Comput.*, vol. 2018, pp. 1–9, Jan. 2018.

[35] S. Imbert, X. Leturc, and C. J. Le Martret, "On the simulation of correlated mobile-to-mobile fading channels for time-varying velocities," in *Proc. Int. Conf. Mil. Commun. Inf. Syst. (ICMCIS)*, Warsaw, Poland, May 2018, pp. 1–8.

[36] Z. Xu, L. Bernadó, M. Gan, M. Hofer, T. Abbas, V. Shivaldova, K. Mahler, D. Smely, and T. Zemen, "Relaying for IEEE 802.11 p at road intersection using a vehicular non-stationary channel model," in *Proc. IEEE 6th Int. Symp. Wireless Veh. Commun. (WiVeC)*, Sep. 2014, pp. 1–6.

[37] P. Paschalidis, J. Nuckelt, K. Mahler, M. Peter, A. Kortke, M. Wisotzki, W. Keusgen, and T. Kürner, "Investigation of MPC correlation and angular characteristics in the vehicular urban intersection channel using channel sounding and ray tracing," *IEEE Trans. Veh. Technol.*, vol. 65, no. 8, pp. 5874–5886, Aug. 2016.

[38] K. Mahler, W. Keusgen, F. Tufvesson, T. Zemen, and G. Caire, "Measurement-based wideband analysis of dynamic multipath propagation in vehicular communication scenarios," *IEEE Trans. Veh. Technol.*, vol. 66, no. 6, pp. 4657–4667, Jun. 2017.

[39] T. Abbas, J. Nuckelt, T. Kürner, T. Zemen, C. F. Mecklenbräuker, and F. Tufvesson, "Simulation and measurement-based vehicle-to-vehicle channel characterization: Accuracy and constraint analysis," *IEEE Trans. Antennas Propag.*, vol. 63, no. 7, pp. 3208–3218, Jul. 2015.

[40] K. Mahler, P. Paschalidis, A. Kortke, M. Peter, and W. Keusgen, "Realistic IEEE 802.11 p transmission simulations based on channel sounder measurement data," in *Proc. IEEE 78th Veh. Technol. Conf. (VTC Fall)*, Sep. 2013, pp. 1–5.

[41] F. Talebi and T. Pratt, "Channel sounding and parameter estimation for a wideband correlation-based MIMO model," *IEEE Trans. Veh. Technol.*, vol. 65, no. 2, pp. 499–508, Feb. 2015.

[42] S. Salous, *Radio Propagation Measurement and Channel Modeling*, 1st ed. Hoboken, NJ, USA: Wiley, 2013.

[43] N. Costa and S. Haykin, *Multiple-Input Multiple-Output Channel Models: Theory and Practice*, 1st ed. Hoboken, NJ, USA: Wiley, 2010.

[44] B. Sklar, "Rayleigh fading channels in mobile digital communication systems. I. Characterization," *IEEE Commun. Mag.*, vol. 35, no. 7, pp. 90–100, Jul. 1997.
[45] L. Bernadö, T. Zemen, F. Tufvesson, A. F. Molisch, and C. F. Mecklenbräuker, "Delay and Doppler spreads of nonstationary vehicular channels for safety-relevant scenarios," *IEEE Trans. Veh. Technol.*, vol. 63, no. 1, pp. 82–93, Jan. 2014.
[46] L. Bernado, T. Zemen, F. Tufvesson, A. F. Molisch, and C. F. Mecklenbrauker, "The (in-)validity of the WSSUS assumption in vehicular radio channels," in *Proc. IEEE 23rd Int. Symp. Pers., Indoor Mobile Radio Commun. (PIMRC)*, Sidney, NSW, Australia, Sep. 2012, pp. 1757–1762.
[47] M. Rice, W. Harrison, B. Jensen, K. Norman, B. Wood, and C. A. Gutierrez, "V2V propagation in mountainous terrain: Part I—Experimental configuration and measurement results," in *Proc. IEEE Latin-Amer. Conf. Commun. (LATINCOM)*, Nov. 2019, pp. 1–6.
[48] C. A. Gutierrez, W. Harrison, and M. Rice, "V2V propagation in mountainous terrain: Part II—Modeling results," in *Proc. IEEE Latin-Amer. Conf. Commun. (LATINCOM)*, Nov. 2019, pp. 1–6.
[49] H. Fernández, L. Rubio, V. M. Rodrigo-Peñarrocha, and J. Reig, "Path loss characterization for vehicular communications at 700 MHz and 5.9 GHz under LOS and NLOS conditions," *IEEE Antennas Wireless Propag. Lett.*, vol. 13, pp. 931–934, 2014.
[50] C. A. G. Vega, C. A. Gutiérrez, J. J. J. Rodriguez, J. V. Castillo, D. U. C. Delgado, J. M. L. Rivera, and M. A. D. Ibarra, "Doppler spectrum measurements of vehicular radio channels using a narrowband sounder," *Revista Facultad Ingeniería Universidad Antioquia*, no. 93, pp. 32–40, Oct./Dec. 2019.
[51] A. Paier, J. Karedal, N. Czink, H. Hofstetter, C. Dumard, T. Zemen, F. Tufvesson, A. F. Molisch, and C. F. Mecklenbräuker, "Car-to-car radio channel measurements at 5 GHz: Pathloss, power-delay profile, and delay-Doppler spectrum," in *Proc. IEEE 4th Int. Symp. Wireless Commun. Syst.*, Oct. 2007, pp. 224–228.
[52] A. Paier, L. Bernadó, J. Karedal, O. Klemp, and A. Kwoczek, "Overview of vehicle-to-vehicle radio channel measurements for collision avoidance applications," in *Proc. IEEE 71st Veh. Technol. Conf.*, May 2010, pp. 1–5.
[53] *IEEE Standard for Information Technology—Local and Metropolitan Area Networks—Specific Requirements—Part 11: Wireless LAN Medium Access Control (MAC) and Physical Layer (PHY) Specifications Amendment 6: Wireless Access in Vehicular Environments*, IEEE Standard 802.11-2007, 2010.
[54] R. Sevlian, C. Chun, I. Tan, A. Bahai, and K. Laberteaux, "Channel characterization for 700 MHz DSRC vehicular communication," *J. Electr. Comput. Eng.*, vol. 2010, pp. 1–9, Jul. 2010.
[55] L. Cheng, B. Henty, D. D. Stancil, F. Bai, and P. Mudalige, "A fully mobile, GPS enabled, vehicle-to-vehicle measurement platform for characterization of the 5.9 GHz DSRC channel," in *Proc. IEEE Antennas Propag. Soc. Int. Symp.*, Jun. 2007, pp. 2005–2008.
[56] L. Cheng, B. E. Henty, D. D. Stancil, F. Bai, and P. Mudalige, "Mobile vehicle-to-vehicle narrow-band channel measurement and characterization of the 5.9 GHz dedicated short range communication (DSRC) frequency band," *IEEE J. Sel. Areas Commun.*, vol. 25, no. 8, pp. 1501–1516, Oct. 2007.
[57] Y. Shmaliy, *Continuous-Time Systems*. Dordrecht, The Netherlands: Springer, 2007.
[58] J. S. Bendat and A. G. Piersol, *Random Data Analysis and Measurement Procedures*, 3rd ed. New York, NY, USA: Wiley, 2000.
[59] M. Pätzold, *Mobile Radio Channels*, 2nd ed. Chichester, U.K.: Wiley, 2011.
[60] P. A. Bello, "Characterization of randomly time-variant linear channels," *IEEE Trans. Commun. Syst.*, vol. CS-11, no. 4, pp. 360–393, Dec. 1963.
[61] G. Matz, "On non-WSSUS wireless fading channels," *IEEE Trans. Wireless Commun.*, vol. 4, no. 5, pp. 2465–2478, Sep. 2005.
[62] M. Z. Win and R. A. Scholtz, "Impulse radio: How it works," *IEEE Commun. Lett.*, vol. 2, no. 2, pp. 36–38, Feb. 1998.
[63] M. Z. Win and R. A. Scholtz, "Ultra-wide bandwidth time-hopping spread-spectrum impulse radio for wireless multiple-access communications," *IEEE Trans. Commun.*, vol. 48, no. 4, pp. 679–689, Apr. 2000.
[64] D. Cassioli, M. Z. Win, and A. F. Molisch, "The ultra-wide bandwidth indoor channel: From statistical model to simulations," *IEEE J. Sel. Areas Commun.*, vol. 20, no. 6, pp. 1247–1257, Aug. 2002.
[65] M. Z. Win and R. A. Scholtz, "Characterization of ultra-wide bandwidth wireless indoor channels: A communication-theoretic view," *IEEE J. Sel. Areas Commun.*, vol. 20, no. 9, pp. 1613–1627, Dec. 2002.
[66] M. Chiani, A. Conti, and O. Andrisano, "Outage evaluation for slow frequency-hopping mobile radio systems," *IEEE Trans. Commun.*, vol. 47, no. 12, pp. 1865–1874, Dec. 1999.
[67] H. Schulze and C. Lüders, *Theory and Applications of OFDM and CDMA Wideband Wireless Communications*. Chichester, U.K.: Wiley, 2005.
[68] F. Zabini, B. M. Masini, A. Conti, and L. Hanzo, "Partial equalization for MC–CDMA systems in non-ideally estimated correlated fading," *IEEE Trans. Veh. Technol.*, vol. 59, no. 8, pp. 3818–3830, Oct. 2010.
[69] A. Conti, B. Masini, F. Zabini, and O. Andrisano, "On the down-link performance of multi-carrier CDMA systems with partial equalization," *IEEE Trans. Wireless Commun.*, vol. 6, no. 1, pp. 230–239, Jan. 2007.
[70] M. Chiani, A. Conti, and C. Fontana, "Improved performance in TD-CDMA mobile radio system by optimizing energy partition in channel estimation," *IEEE Trans. Commun.*, vol. 51, no. 3, pp. 352–355, Mar. 2003.
[71] E. Salazar, C. A. Azurdia-Meza, D. Zabala-Blanco, S. Bolufé, and I. Soto, "Semi-supervised extreme learning machine channel estimator and equalizer for vehicle to vehicle communications," *Electronics*, vol. 10, no. 8, p. 968, Apr. 2021.
[72] A. Conti, M. Z. Win, and M. Chiani, "Slow adaptive M-QAM with diversity in fast fading and shadowing," *IEEE Trans. Commun.*, vol. 55, no. 5, pp. 895–905, May 2007.
[73] L. Toni and A. Conti, "Does fast adaptive modulation always outperform slow adaptive modulation?" *IEEE Trans. Wireless Commun.*, vol. 10, no. 5, pp. 1504–1513, May 2011.
[74] M. Patzold and N. Youssef, "Spectrogram analysis of multipath fading channels," in *Proc. IEEE 26th Annu. Int. Symp. Pers., Indoor, Mobile Radio Commun. (PIMRC)*, Aug. 2015, pp. 2214–2219.
[75] C. A. Gutierrez, M. Patzold, N. M. Ortega, C. A. Azurdia-Meza, and F. M. Maciel-Barboza, "Doppler shift characterization of wideband mobile radio channels," *IEEE Trans. Veh. Technol.*, vol. 68, no. 12, pp. 12375–12380, Dec. 2019.
[76] C. Rauscher, V. Janssen, and R. Minihold, *Fundamentals of Spectrum Analysis*, 5th ed. Munich, Germany: Rohde & Schwarz, 2007.
[77] C. A. Hammerschmidt, R. T. Johnk, P. M. McKenna, and C. R. Anderson, "Best practices for radio propagation measurements," NTIA, Washington, DC, USA, Tech. Rep., Memorandum TM-19-535, 2018.
[78] *Keysight N9310A Signal Generator*, 3rd ed. Chengdu, China: Keysight Technol., 2014.
[79] *Keysight FieldFox Analyzers: User's Guide*, 4th ed. Santa Rosa, CA, USA: Keysight Technol., 2017.

CARLOS A. GÓMEZ-VEGA (Graduate Student Member, IEEE) received the M.S. degree in electronic engineering from the Universidad Autónoma de San Luis Potosí, San Luis Potosí, Mexico, in 2020. He is currently pursuing the Ph.D. degree with the Wireless Communication and Localization Networks Laboratory, University of Ferrara, Italy.

Since 2020, he has been a Research Assistant with the Wireless Communication and Localization Networks Laboratory, University of Ferrara. In 2019, he was a Visiting Student with the Wireless Information and Network Sciences Laboratory, Massachusetts Institute of Technology, USA. His current research interests include network localization and navigation, and wireless resource optimization.

Mr. Gómez-Vega received the Best Paper Award from the IEEE LATINCOM in 2019. He also serves as a reviewer for various IEEE journals and international conferences.

JORGE CARDENAS (Student Member, IEEE) received the B.S. degree in electronics engineering from the Universidad Autónoma de San Luis Potosí, Mexico, in 2016, and the M.S. degree in applied science from the Optical Communications Research Institute, Mexico, in 2018. He is currently pursuing the Ph.D. degree in engineering sciences with the Universidad Autónoma de San Luis Potosí. His current research interests include machine learning, fall detection, and vehicle-to-vehicle communications.

JUAN C. ORNELAS-LIZCANO received the B.S. degree in physics from the Universidad Autónoma de San Luis Potosí, Mexico, in 2009, the M.Eng. degree in electrical engineering from the Universidad de Guanajuato, in 2011, the B.S. degree in electronics engineering from the Instituto Tecnológico de San Luis Potosí, in 2013, and the Ph.D. degree in engineering and science in materials from the Universidad Autónoma de San Luis Potosí, in 2018, where he is currently pursuing the Ph.D. degree in electronics engineering.

His current research interests include wireless communications and vehicular communications.

CARLOS A. GUTIÉRREZ (Senior Member, IEEE) received the B.E. degree in electronics and digital communication systems from the Universidad Autónoma de Aguascalientes, Mexico, in 2002, the Advanced Studies Diploma degree in signal processing and communication theory from the Universidad Politécnica de Cataluña, Spain, in 2005, the M.S. degree in electronics and telecommunications from CICESE, Mexico, in 2006, and the Ph.D. degree in mobile communication systems from the University of Agder, Norway, in 2009.

From 2009 to 2011, he was with the School of Engineering, Universidad Panamericana, Aguascalientes, Mexico. Since January 2012, he has been with the Faculty of Science, Universidad Autónoma de San Luis Potosí, Mexico. His research interests include modeling, simulation, and measurement of wireless channels; antenna design; vehicular communications; and wireless perception systems for human activity recognition.

Dr. Gutiérrez is a member of the Mexican National System of Researchers. His publications received three best paper awards. He has held different positions in organizing and technical program committees of various international conferences. He has served as an Expert Evaluator for the European Commission and CONACYT (Mexico); an Associate Editor for the *IEEE Vehicular Technology Magazine*; an Academic Editor for *Mobile Information Systems*; and a Guest Editor for *Wireless Communications and Mobile Computing*, *Modelling and Simulation in Engineering*, and the IEEE Latin America Transactions.

MARCO CARDENAS-JUAREZ (Senior Member, IEEE) received the B.Sc. degree in electronic engineering from the Autonomous University of San Luis Potosí (UASLP), Mexico, in 2002, the M.Sc. degree in electronic engineering (major in telecommunications) from the Monterrey Institute of Technology and Higher Education (ITESM) at Monterrey, Mexico, in 2004, and the Ph.D. degree in electronic and electrical engineering from the University of Leeds, U.K., in 2012. Since 2003, he has been a Lecturer at different public and private universities in Mexico. In 2013, he was a Postdoctoral Research Associate with the French-Mexican Laboratory for Informatics and Automatics Control, Center for Research and Advanced Studies of the National Polytechnic Institute (CINVESTAV), Mexico. Since 2014, he has been an Associate Professor with the Faculty of Sciences, UASLP, where he has been the Coordinator of the B.Sc. program in telecommunications engineering since 2016. His research interest includes signal processing for wireless communications. He has been a member of the Mexican National System of Researchers since 2015. He serves as an Associate Section Editor for the *Journal of Applied Research and Technology* of the National Autonomous University of Mexico (UNAM).

JOSÉ M. LUNA-RIVERA received the B.S. and M.Eng. degrees in electronics engineering from the Autonomous University of San Luis Potosi, Mexico, in 1997 and 1998, respectively, and the Ph.D. degree in electrical engineering from The University of Edinburgh, U.K., in 2003. He is currently a full-time Professor with the Faculty of Sciences, Autonomous University of San Luis Potosi. His research interests include applying signal processing for wireless communication systems, including developing techniques and algorithms for array signal detection, efficient modulation schemes, transmit/receive diversity schemes, channel modeling, signal precoding, interference cancellation, and power control techniques. Applications of this research work include visible light communications, vehicular communications, the Internet of Things, and mobile communications, which resulted in over 100 journals and refereed conference publications. In 2014, he received the University Award for Technological and Scientific Research as a Young Researcher from the Autonomous University of San Luis Potosi.

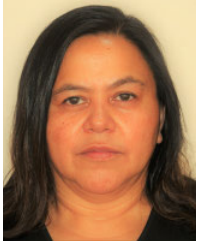

RUTH M. AGUILAR-PONCE (Member, IEEE) received the B.S. degree in computer science from the Autonomous University of Puebla, Mexico, in 1997, the M.S. degree in electronics from the National Institute for Research in Optics, Astrophysics and Electronics, Mexico, in 1999, and the M.S. degree in computer engineering and the Ph.D. degree from the University of Louisiana at Lafayette, in 2004 and 2007, respectively. She joined the Center for Advanced Computer Studies, University of Louisiana at Lafayette. She is currently an Assistant Professor with the Autonomous University of San Luis Potosi, Mexico. Her research interests include sensor networks, video processing, signal and image processing, and embedded system design.